

Cyclic 2.5D Perceptual Loss for Cross-Modal 3D Medical Image Synthesis: T1w MRI to Tau PET

Junho Moon^a, Symac Kim^b, Haejun Chung^{a,b,c,†}, Ikbeom Jang^{d,e,f,†}, for the Alzheimer’s Disease Neuroimaging Initiative*

^a*Department of Artificial Intelligence Semiconductor Engineering, Hanyang University, Seoul, South Korea*

^b*Department of Artificial Intelligence, Hanyang University, Seoul, South Korea*

^c*Department of Electronic Engineering, Hanyang University, Seoul, South Korea*

^d*Division of Computer Engineering, Hankuk University of Foreign Studies, Yongin, South Korea*

^e*Division of AI Data Convergence, Hankuk University of Foreign Studies, Yongin, South Korea*

^f*Division of Language & AI, Hankuk University of Foreign Studies, Yongin, South Korea*

Abstract

There is a demand for medical image synthesis or translation to generate synthetic images of missing modalities from available data. This need stems from challenges such as restricted access to high-cost imaging devices, government regulations, or failure to follow up with patients or study participants. In medical imaging, preserving high-level semantic features is often more critical than achieving pixel-level accuracy. Perceptual loss functions are widely employed to train medical image synthesis or translation models, as they quantify differences in high-level image features using a pre-trained feature extraction network. While 3D and 2.5D perceptual losses are used in 3D medical image synthesis, they face challenges, such as the lack of pre-trained 3D models or difficulties in balancing loss reduction across different planes. In this work, we focus on synthesizing 3D tau PET images from 3D T1-weighted MR images. We propose a cyclic 2.5D perceptual loss that sequentially computes the 2D average perceptual loss for each of the axial, coronal, and sagittal planes over epochs, with the cycle duration gradually decreasing. Additionally, we process tau PET images using by-manufacturer standardization to enhance the preservation of high-SUVR regions indicative of tau pathology and mitigate SUVR variability caused by inter-manufacturer differences. We combine the proposed loss with SSIM and MSE losses and demonstrate its effectiveness in improving both quantitative and qualitative performance across various generative models, including U-Net, UNETR, SwinUNETR, CycleGAN, and Pix2Pix.

Keywords: Cyclic 2.5D perceptual loss, PET, MRI, Image synthesis, Image translation

[†]Corresponding authors

Email addresses: haejun@hanyang.ac.kr (Haejun Chung), ijang@hufs.ac.kr (Ikbeom Jang)

*Data used in preparation of this article were obtained from the Alzheimer’s Disease Neuroimaging Initiative (ADNI) database (adni.loni.usc.edu). As such, the investigators within the ADNI contributed to the design and implementation of ADNI and/or provided data but did not participate in analysis or writing of this report. A complete listing of ADNI investigators can be found at: http://adni.loni.usc.edu/wp-content/uploads/how_to_apply/ADNI_Acknowledgement_List.pdf

1. Introduction

Medical image synthesis or translation enables the generation of synthetic images for missing modalities using available data. Medical imaging is essential in clinical practice, with different modalities offering distinct clinical capabilities (Yu et al., 2020; Nie et al., 2018). By considering multiple modalities, complementary data can be integrated, enhancing diagnostic efficiency through improved accuracy in disease diagnosis and aiding in the characterization of lesions (Ortner et al., 2019; Zhu and Zhu, 2019; Du et al., 2016). In computer-aided diagnosis, the problem of incomplete data due to missing modalities significantly reduces the size of the training set available for model development, ultimately impairing diagnostic performance (Pan et al., 2020). Thus, the capability of medical image synthesis to obtain absent modalities is highly demanded in clinical environments.

Synthesizing positron emission tomography (PET) images from magnetic resonance imaging (MRI) is particularly challenging among these tasks. Alzheimer’s Disease (AD) is the most prevalent form of dementia that causes cognitive impairment (Knopman et al., 2021). Currently, there is no cure and no effective treatment for AD; only palliative care is available, and long-term therapeutic options remain limited (Wang et al., 2022; Winblad et al., 2016; Jack Jr et al., 2018). Therefore, early diagnosis is crucial to improve the prognosis, preserve cognitive function (Rasmussen and Langerman, 2019), and reduce both direct and indirect costs associated with care (Wong, 2020). AD is characterized by beta-amyloid plaques and neurofibrillary tangles (NFTs) with tau protein (Knopman et al., 2021; Buchhave et al., 2012). Tau PET can detect and visualize the accumulation of abnormally phosphorylated tau proteins that form NFTs within the brain (Pooler et al., 2013). In early-stage patients, high NFT accumulation is visualized through tau PET in the entorhinal cortex, which progresses to the cerebral regions such as the hippocampus and eventually appears throughout the entire neocortex in late-stage AD (Pooler et al., 2013; Cho et al., 2016). Consequently, visualizing NFT is critical for the diagnosis of AD, and tau PET offers higher sensitivity compared to MRI for this purpose as it directly targets these accumulations.

Despite its diagnostic utility, tau PET imaging presents several limitations that hinder its routine implementation in clinical settings. The procedure involves the intravenous administration of radioactive tracers (Gambhir, 2002; Guo et al., 2021), rendering it inherently invasive. In addition, PET imaging is associated with considerable financial costs—often reaching several thousand USD per scan (Berger et al., 2003; Dietlein et al., 2000; Buck et al., 2010). Access to this modality is largely confined to specialized medical centers, thereby limiting its availability to the broader patient population (Saif et al., 2010; Slough et al., 2016). Furthermore, incorporating tau PET into the standard diagnostic workflow for dementia—which may already involve structural MRI, FDG-PET, and amyloid PET—adds procedural complexity and increases patient burden, including cumulative exposure to multiple radiopharmaceutical agents (Lee et al., 2024). Although tau PET is regarded as an *attractive biomarker* for Alzheimer’s disease, it remains *not readily accessible* to most patients.

Given these challenges, the development of surrogate imaging techniques that leverage more accessible modalities, such as MRI, to approximate PET imaging has garnered increasing attention. Such methods hold the potential to reduce reliance on PET by mitigating issues related to cost, invasiveness, and availability—while still providing critical molecular-

level insights. In this study, we specifically focus on synthesizing tau PET images from T1-weighted (T1w) MRI. Recent studies have explored synthesizing PET images from MRI using deep learning approaches (Jang et al., 2023; Shin et al., 2020; Zhang et al., 2022). Since maintaining high-level semantic information is critical in medical image synthesis, various approaches (Zhao et al., 2021; Hu et al., 2021), employ perceptual loss (Johnson et al., 2016) as a component of their combined loss, as it allows addressing perceptual difference and preventing the generation of blurry images (Johnson et al., 2016; Armanious et al., 2020) unlike traditional per-pixel losses. For 3D medical environments, both 3D and 2.5D perceptual losses are applicable; however, each approach has limitations. The 3D approach may struggle to capture spatial information across the axial, coronal, and sagittal planes comprehensively—information crucial for clinical applications—and is further constrained by the limited availability of pre-trained 3D models. The 2.5D approach, on the other hand, faces challenges in reducing each 2D plane-wise perceptual loss in a balanced manner.

To tackle these problems, we introduce a cyclic 2.5D perceptual loss for 3D medical image synthesis, as illustrated in Figure 1. This method sequentially calculates 2D perceptual losses for the axial, coronal, and sagittal planes, allocating an equal number of epochs to each plane per cycle. As training progresses, the cycles repeat with fewer epochs. Combined with mean squared error (MSE) and structural similarity index measure (SSIM) losses, this method preserves both semantic and structural similarity in the generated images. In addition, we incorporate a by-manufacturer standardization approach to address variations in standardized uptake value ratio (SUVR) distributions across PET images from different manufacturers. It helps retain critical high-SUVR focal areas, improving the quality of synthesized images by preserving important features that min-max normalization might otherwise diminish. Our approach is applied to deep generative models, including a 3D U-Net (Çiçek et al., 2016) and its variants such as UNETR (Hatamizadeh et al., 2022), SwinUNETR (Hatamizadeh et al., 2021), as well as generative adversarial network (GAN) (Goodfellow et al., 2014) based methods like CycleGAN (Zhu et al., 2017) and Pix2Pix (Isola et al., 2017), demonstrating significant performance improvements in both 2D cross-sectional slices and 3D volumetric reconstructions.

2. Related Work

Tau PET. PET imaging detects high-energy photons emitted by positron-emitting radioisotopes, enabling precise in vivo quantification of radiotracer concentrations (Vaquero and Kinahan, 2015). Tau PET is specifically employed for diagnosing tauopathies, including AD and Parkinson’s disease, using dedicated radiotracers (Leuzy et al., 2019). First-generation tau PET radiotracers include $[^{18}\text{F}]\text{THK5317}$, $[^{18}\text{F}]\text{THK5351}$, $[^{18}\text{F}]\text{AV-1451}$ (also referred to as $[^{18}\text{F}]\text{AV-flortaucipir}$), and $[^{11}\text{C}]\text{PBB3}$ (Petersen et al., 2022; Leuzy et al., 2019). Among these, $[^{18}\text{F}]\text{AV-1451}$ was the first to receive FDA approval. This radiotracer exhibits high affinity for tau aggregates with minimal binding to beta-amyloid, effectively crosses the blood-brain barrier, and possesses a favorable metabolic profile (Petersen et al., 2022; Mattay et al., 2020). While its sensitivity is notably high for AD diagnosis, its effectiveness in non-AD tauopathies is comparatively limited (Petersen et al., 2022). Alternative diagnostic methods for AD include cerebrospinal fluid testing (Shaw et al., 2018) and blood plasma analysis (Barthélemy et al., 2024). However, unlike fluid-based biomarkers, tau PET enables

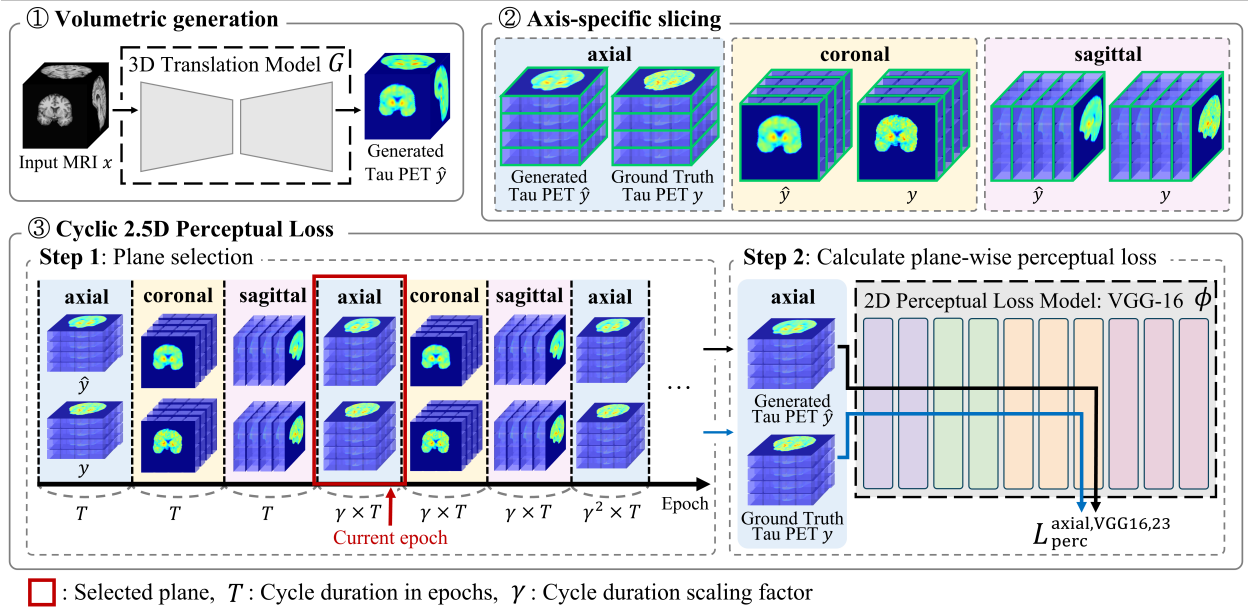


Figure 1: Overview of our proposed cyclic 2.5D perceptual loss. Following the generation of a 3D tau PET image from the given 3D T1w MR image, both the generated tau PET image \hat{y} and the ground truth tau PET image y are sliced into axial, coronal, or sagittal planes based on the current epoch. The sliced image pairs are then processed through the first 23 layers of a pre-trained VGG-16 model, and the corresponding feature maps are extracted. For each slice pair, the mean squared error between the paired feature maps is computed and averaged.

direct visualization of NFTs in the brain, facilitating the assessment of disease phenotypes, progression stages, and pathological localization.

Perceptual Loss. Johnson et al. (2016) argued that traditional per-pixel loss functions are insufficient for capturing perceptual differences in images. To address these limitations, they introduced feature reconstruction loss and style reconstruction loss. Feature reconstruction loss, commonly referred to as perceptual loss (Liu et al., 2021), evaluates the similarity between feature maps of a pre-trained model, such as VGG (Simonyan and Zisserman, 2015), for the ground truth and generated images. This loss is computed using the average squared Euclidean distance, as defined below:

$$L_{\text{perc}}^{\phi,j}(\hat{y}, y) = \frac{1}{C_j H_j W_j} \|\phi_j(\hat{y}) - \phi_j(y)\|_2^2, \quad (1)$$

where y represents the ground truth image, \hat{y} denotes the generated image, ϕ refers to the pre-trained model, j is the layer index in ϕ , and C_j , H_j , W_j are the number of channels, height, and width of the feature map, respectively.

For 3D images, perceptual loss can be computed using two different approaches: the 3D and the 2.5D approaches. In the 3D approach, perceptual loss is calculated using a pre-trained 3D model, which incorporates the depth dimension D_j . The 3D perceptual loss is formulated as follows:

$$L_{\text{3Dperc}}^{\phi,j}(\hat{y}, y) = \frac{1}{C_j H_j W_j D_j} \|\phi_j(\hat{y}) - \phi_j(y)\|_2^2. \quad (2)$$

The 2.5D approach computes perceptual loss by aggregating 2D perceptual losses across three orthogonal planes: axial, coronal, and sagittal. This method utilizes a pre-trained 2D model, such as VGG (Ha et al., 2024), to extract feature representations from each plane independently. The perceptual losses computed for each plane are then combined to approximate the 3D structural context. The 2.5D perceptual loss is represented as follows:

$$L_{2.5D_{\text{perc}}}^{\phi,j}(\hat{y}, y) = L_{\text{perc}}^{\text{axial},\phi,j}(\hat{y}, y) + L_{\text{perc}}^{\text{coronal},\phi,j}(\hat{y}, y) + L_{\text{perc}}^{\text{sagittal},\phi,j}(\hat{y}, y). \quad (3)$$

Here, $L_{\text{perc}}^{\text{axial},\phi,j}(\hat{y}, y)$, $L_{\text{perc}}^{\text{coronal},\phi,j}(\hat{y}, y)$, and $L_{\text{perc}}^{\text{sagittal},\phi,j}(\hat{y}, y)$ are the 2D perceptual losses computed along the axial, coronal, and sagittal planes, respectively.

Cross-Modality Brain Image Synthesis with Deep Learning. Cross-modality image synthesis aims to learn the relationship between input and target images to generate realistic images in a different modality or contrast. In brain imaging, this technique is primarily used to synthesize images in different modalities (e.g., MRI, PET) or contrasts (e.g., T1-weighted, diffusion-weighted imaging) from available scans. Clinically, it offers significant benefits, such as reducing scanner time and imaging costs, while deep learning enables high-quality synthesis despite the complex nonlinear mappings between modalities (Dayarathna et al., 2023). Several backbone models have been employed for cross-modality synthesis, including CycleGAN (e.g., Yang et al. 2018; Abu-Srhan et al. 2021), U-Net (Ronneberger et al., 2015) (e.g., Sikka et al. 2018), and Denoising Diffusion Probabilistic Models (Ho et al., 2020) (e.g., Pan et al. 2023; Xie et al. 2023). Some approaches incorporate perceptual loss or similar loss functions as part of their composite loss formulation to enhance perceptual fidelity (Armanious et al., 2019; Dar et al., 2019).

Various approaches have been developed for translating medical images into PET images. GANDALF (Shin et al., 2020) introduced a conditional generative adversarial network with discriminator-adaptive loss fine-tuning to synthesize ^{18}F AV-45 and ^{18}F FDG PET images from T1w MRI scans while simultaneously classifying AD. BPGAN (Zhang et al., 2022) demonstrated T1w MRI to ^{18}F FDG PET image translation using conditional variational autoencoder GAN and conditional latent regressor GAN with multiple loss functions including SSIM loss. TauPETGen (Jang et al., 2023) is a latent diffusion model-based approach to generate ^{18}F MK-6420 PET from text-written MMSE values and/or an MRI. Wang et al. (2024) proposed a joint learning framework to enhance the early diagnosis of AD. This framework comprises ShareGAN for cross-modal synthesis of T1w MR images and ^{18}F FDG PET images, as well as a diagnosis network for AD detection. By jointly training these components, the framework effectively improves AD diagnostic performance. PASTA (Li et al., 2024) employs a Conditional Diffusion Model-based dual-arm architecture to synthesize ^{18}F FDG PET images from T1w MR images. It incorporates adaptive normalization layers into the dual-arm architecture, allowing for the seamless integration of multi-modal conditions and facilitating the generation of pathology-aware PET images.

3. Methods

3.1. Data Collection and Statistics

We collected 516 pairs of 3D T1w MR and 3D tau PET images from the publicly available Alzheimer’s Disease Neuroimaging Initiative (ADNI) dataset (adni.loni.usc.edu), specifically

| Data Split | Gender (Male/Female) | Age (Min-Max) | Race (White/Black/Others) | Diagnosis (AD/LMCI/MCI/EMCI) |
|-----------------|-------------------------|-------------------------|------------------------------|---------------------------------|
| Total (516) | 291/225 | 74.2±7.9 (55.3-94.0) | 462/31/23 | 97/50/267/102 |
| Train (360) | 206/154 | 73.9±8.0 (55.3-94.0) | 321/22/17 | 66/37/187/70 |
| Validation (78) | 41/37 | 75.5±7.5 (59.4-91.6) | 69/4/5 | 16/8/39/15 |
| Test (78) | 44/34 | 74.7±7.5 (57.4-92.0) | 72/5/1 | 15/5/41/17 |

Table 1: Demographic and clinical characteristics of participants. For the total, training, validation, and test datasets, information on gender, age (mean \pm standard deviation), race, and clinical type (AD, LMCI, MCI, and EMCI) is provided. The ages are based on the MRI retrieval timestamp.

from ADNI 2, ADNI 3, and ADNI 4 study phases. The T1w MRI scans were obtained as original images, whereas the PET scans were classified under the protocol “AV1451 Coreg, Avg, Std Img and Vox Siz, Uniform 6mm Res.” Thus, the signal type of the T1w MR images is raw signal intensity, and the signal type of the tau PET images is SUVR. The radiotracer used in all PET scans was $[^{18}\text{F}]\text{AV-1451}$. The retrieval time differences for all pairs were less than a year. Each subject was categorized into one of the following diagnostic groups: AD, Late Mild Cognitive Impairment (LMCI), Mild Cognitive Impairment (MCI), or Early Mild Cognitive Impairment (EMCI). The dataset was subsequently divided into training, validation, and test subsets, comprising 360, 78, and 78 MRI-PET pairs, respectively. The distribution of the image pairs across these subsets is presented in Table 1.

3.2. Data Preprocessing and Augmentation

Figure 2 illustrates the data preprocessing pipeline. **FreeSurfer (version 7.4.1)** (The General Hospital Corporation (MGH), 2023), a software suite for neuroimage analysis and visualization, was used for preprocessing. Preprocessing began with nonparametric non-uniformity intensity (N3) normalization (Sled et al., 1998) using the `mri_nu_correct.mni` command, followed by initial intensity normalization (Dale et al., 1999) using the `mri_normalize` command. After normalization, the MR images were cropped into cubic (x^3) dimensions. Slices with minimal voxel values at the beginning and end of the scans were removed to prevent distortion of relevant anatomical structures during resizing. Skull stripping and removal of extraneous tissues were performed using Synthstrip (Hoopes et al., 2022) via the `mri_synthstrip` command. Finally, the MR images were resized to $128 \times 128 \times 128$, and intensity values were normalized to the range $(-1, 1)$ using min-max normalization.

The acquired tau PET images were preprocessed following the protocol outlined in the previous section. This process included noise reduction through smoothing, coregistration to align PET images with the baseline fluorodeoxyglucose (FDG) PET scan, and frame averaging. The images were then aligned to the anterior commissure–posterior commissure (AC-PC) plane and transformed into Talairach space using the FDG PET scan as a reference. Intensity normalization was performed relative to the cerebellar gray matter, followed by adaptive smoothing. After these preprocessing steps, skull stripping was conducted using

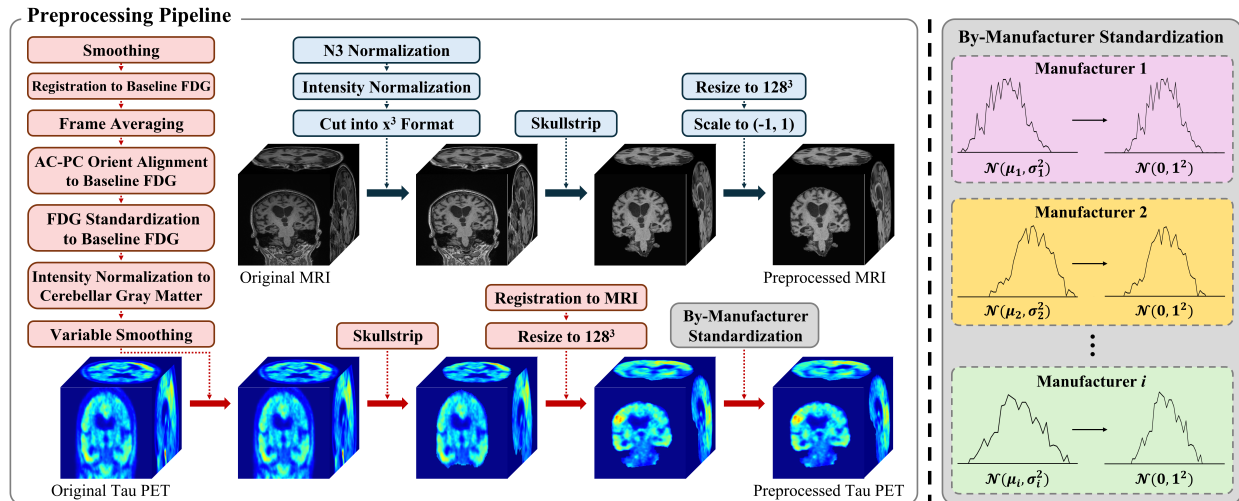


Figure 2: Overall data preprocessing procedures for T1w MR and tau PET images, including the by-manufacturer standardization of tau PET SUVR. The tau PET images were preprocessed through noise reduction via smoothing, spatial coregistration to baseline FDG PET, motion correction through frame averaging, alignment to the AC-PC plane, transformation into Talairach space, intensity normalization using the cerebellar gray matter, and adaptive smoothing. The T1w MRI preprocessing included nonparametric non-uniformity intensity normalization, Freesurfer intensity normalization, and conversion to a cubic format. Extraneous tissues and skulls were removed from the T1w MR and tau PET images. The tau PET images were subsequently co-registered with their corresponding T1w MR images. The intensities of the T1w MR images were scaled to a range of -1 to 1, while the tau PET SUVR values were standardized to a mean of 0 and a standard deviation of 1, adjusted according to the scanner manufacturer.

the `mri_synstrip` command in FreeSurfer. The PET images were then registered to their corresponding MR images using FreeSurfer’s `mri_coreg` and `mri_vol2vol` commands. Finally, the registered PET images were resized to $128 \times 128 \times 128$ to match the dimensions of the MR images.

To account for variability in SUVR measurements caused by differences in PET scanners across manufacturers, we standardized the SUVR values of PET images to have a mean of 0 and a standard deviation of 1, based on manufacturer metadata. Min-max normalization is unsuitable for PET images, as it may suppress or eliminate regions with elevated SUVR, which are crucial for detecting tau accumulation. As illustrated in Figure 3, SUVR values within datasets from the same manufacturer showed distinct patterns across patient groups. Individuals with AD exhibited the highest 99th, 90th, and 75th percentile SUVR values in cortical regions. These values were consistently higher compared to those observed in individuals with MCI, encompassing early, mild, and late stages. This trend aligns with expected biological differences. However, these percentile values varied across manufacturers for both AD and non-AD groups. Despite the internal consistency observed within each manufacturer’s dataset, significant statistical differences ($p < 0.001$) were found in SUVR distributions across cortical regions when comparing PET scanners from different manufacturers (Table 2). This finding suggests that scanner-specific variations impact the direct comparability of SUVR values. These discrepancies indicate that global normalization techniques, such as min-max normalization, may distort biologically meaningful SUVR patterns due to manufacturer-dependent scaling differences. Given that SUVR distributions

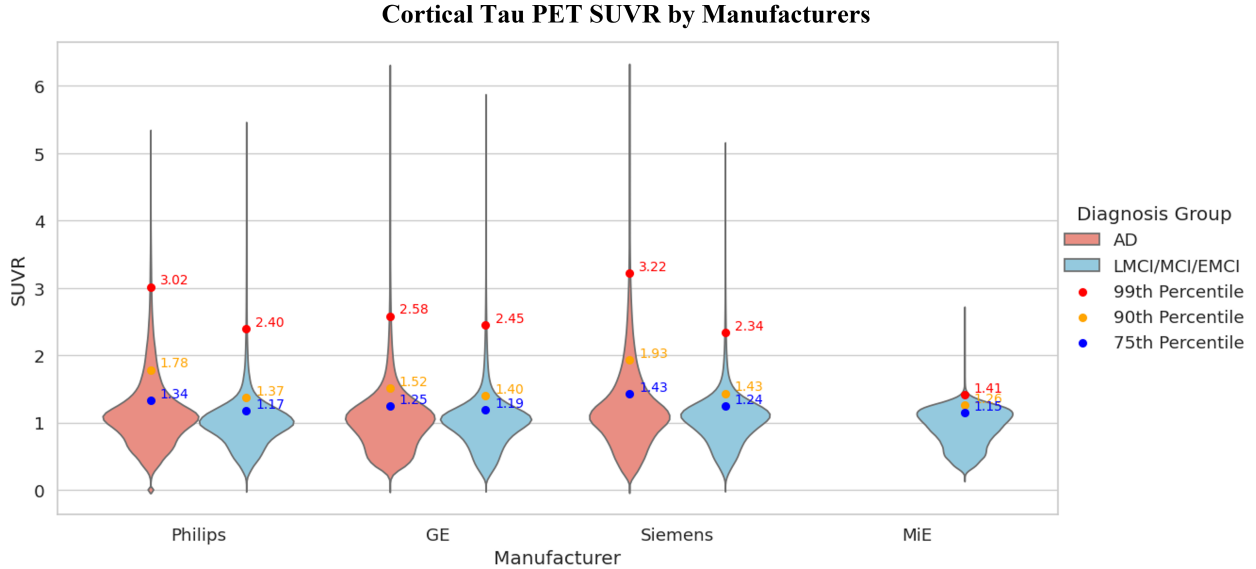


Figure 3: Cortical tau PET SUVR by manufacturers. The tau PET SUVR distribution across different manufacturers is presented for cortical regions, comparing participants with AD to those in the LMCI/MCI/EMCI group. The visualization depicts SUVR values at the 99th, 90th, and 75th percentiles. Across all manufacturers, SUVR values at these percentiles are consistently higher in AD participants than in the LMCI/MCI/EMCI group. Notably, the 99th percentile SUVR values vary across manufacturers in both groups. In all manufacturers, most SUVR values are concentrated around a lower range, approximately 1. Data from the MiE manufacturer for AD participants were unavailable in the collected dataset; thus, the corresponding SUVR distribution is not displayed. The cortical regions were defined using the Desikan-Killiany atlas.

in cortical regions are highly skewed and do not meet the assumptions of normality, we first conducted a non-parametric Kruskal–Wallis H test, which confirmed statistically significant differences in rank distributions among groups. Subsequently, post-hoc pairwise comparisons were performed using the Mann–Whitney U test with Benjamini-Hochberg correction for multiple testing, revealing highly significant differences in SUVR distributions across all patient groups.

Data augmentations were applied randomly at each epoch to enhance the robustness of the model. 3D random elastic deformation was performed using `monai.transforms.Rand3DElasticd` from MONAI (version 1.3.2) (Cardoso et al., 2022). The transformation used trilinear interpolation, a magnitude range of 50–100, zero reflection mode, and a Gaussian kernel with a sigma range of 4 to 7. Additionally, random affine transformations were applied using `monai.transforms.RandAffined`. These included rotations between -15° and 15° and scaling within $\pm 10\%$ along each axis (x, y, z). Random flips along all axes were performed using `monai.transforms.RandFlipd`. Each augmentation was applied with a probability of 0.5 and was consistently applied to both MR and PET images in each paired dataset. To improve robustness against MRI artifacts, Gaussian noise with a mean of 0 and a standard deviation of 1 was added to the MR images.

| Hypothesis test | Comparison | p -value | |
|------------------|---------------------|------------|---------------|
| | | AD | LMCI/MCI/EMCI |
| Kruskal-Wallis H | Overall group | < 0.001 | < 0.001 |
| | Siemens vs. GE | < 0.001 | < 0.001 |
| | Siemens vs. Philips | < 0.001 | < 0.001 |
| Mann-Whitney U | Siemens vs. MiE | < 0.001 | < 0.001 |
| | GE vs. Philips | < 0.001 | < 0.001 |
| | GE vs. MiE | < 0.001 | < 0.001 |
| | Philips vs. MiE | < 0.001 | < 0.001 |

Table 2: Statistical analysis of differences in cortical tau PET SUVR by manufacturers. Hypothesis tests were performed separately for AD patients and a combined group of LMCI, MCI, and EMCI patients. SUVR values were aggregated across all cortical voxels for analysis. Since the SUVR distribution did not meet the assumption of normality, non-parametric hypothesis testing methods were employed. The Kruskal-Wallis H test revealed that, in both the AD and LMCI/MCI/EMCI groups, at least one manufacturer exhibited a statistically significant difference in cortical SUVR distribution compared to others. Post-hoc analysis using pairwise Mann-Whitney U tests, with Benjamini-Hochberg correction for multiple comparisons, confirmed significant differences in cortical SUVR distributions between manufacturers in both groups. The cortical regions were defined using the Desikan-Killiany atlas.

3.3. 3D Image Translation: T1-Weighted MRI to Tau PET

Given a T1w MRI modality X paired with the corresponding tau PET modality Y , our objective is to learn a mapping $G : X \rightarrow Y$ such that $G(x) \approx y$ for each $x \in X$ to its paired $y \in Y$. A 3D image translation model G is trained to minimize the difference between the generated tau PET image \hat{y} and the ground truth tau PET image y by optimizing the objective function described below, with a 3D T1w MRI x as input. The proposed loss function is not specific to a particular model but can be applied to various image-to-image translation models such as U-Net and GANs.

Cyclic 2.5D Perceptual Loss. The cyclic 2.5D perceptual loss, denoted as $L_{\text{perc}}^{\text{plane}, \phi, j}(\hat{y}, y)$, is a *plane*-based perceptual loss derived from the j -th layer of the 2D pre-trained model ϕ . For each pair of the ground truth PET image y and the generated PET image \hat{y} , this loss is computed as detailed in Algorithm 1 and visualized in Figure 1. The implementation of the cyclic 2.5D perceptual loss involves sequentially applying the axial 2D average perceptual loss for T epochs, followed by the coronal 2D average perceptual loss for an equivalent duration, and subsequently the sagittal 2D average perceptual loss for the same number of epochs. This sequence constitutes a single complete cycle, with the duration of each successive cycle adjusted by scaling T by a predefined cycle duration scaling factor γ . The 2D perceptual loss is computed as described in Algorithm 1. However, it differs from the original perceptual loss explained in Section 2 in that it omits the term $\frac{1}{C_j H_j W_j D_j}$. Since all input data share identical dimensions ($128 \times 128 \times 128$) and the output feature maps are obtained from the same layer positions within the model, the values of C_j , H_j , W_j , and D_j remain constant regardless of the input data. Thus, $\frac{1}{C_j H_j W_j D_j}$ can be treated as a constant factor and is therefore excluded from the cyclic 2.5D perceptual loss calculation.

Structural Preservation Loss. We utilized SSIM as a loss function to preserve structural similarity between the generated PET image \hat{y} and the ground truth PET image y . SSIM is a metric that evaluates statistical similarity based on luminance and contrast (Wang

Algorithm 1: Computing Cyclic 2.5D Perceptual Loss

Require: The first j layers of a pre-trained model ϕ ;
ground truth PET $y \in \mathbf{R}^{W \times D \times H}$;
generated PET $\hat{y} \in \mathbf{R}^{W \times D \times H}$;
mean squared error MSE;
selected plane $plane$ from Algorithm 2
Ensure: Cyclic 2.5D perceptual loss $L_{perc}^{plane, \phi, j}(y, \hat{y})$

Get $y_i, \hat{y}_i \leftarrow \text{SLICE}(y, \hat{y}; plane)$ for $i = 1 \dots H$
 $perceptual_loss = 0$
for $i = 1 \dots H$ **do**
 Min-Max Normalize y_i, \hat{y}_i into $(0, 1)$
 $perceptual_loss \leftarrow perceptual_loss + \text{MSE}(\phi_j(y_i), \phi_j(\hat{y}_i))$
end for
return $perceptual_loss/H$

et al., 2004). Given a predetermined window size, a Gaussian filter with a standard deviation of σ is applied, and the window scans across both images, \hat{y} and y . For each window pair, the means $\mu_{\hat{y}}, \mu_y$, variances $\sigma_{\hat{y}}, \sigma_y$, and covariance $\sigma_{\hat{y}y}$ are calculated. SSIM is computed as:

$$\text{SSIM}(\hat{y}, y) = \frac{(2\mu_{\hat{y}}\mu_y + C_1)(2\sigma_{\hat{y}y} + C_2)}{(\mu_{\hat{y}}^2 + \mu_y^2 + C_1)(\sigma_{\hat{y}}^2 + \sigma_y^2 + C_2)}. \quad (4)$$

where $C_1 = (k_1 \cdot L)^2$, $C_2 = (k_2 \cdot L)^2$, L represents the data range, and k_1 and k_2 are set to 0.01 and 0.03, respectively. After the window completes its traversal over the image, the average SSIM value is computed. The window has the same dimensionality as the images. When used as a loss function, the SSIM loss is defined as:

$$L_{\text{SSIM}}(\hat{y}, y) = 1 - \text{SSIM}(\hat{y}, y). \quad (5)$$

Voxel-level Fidelity Loss. In addition, a voxel-wise loss function L_{voxel} is defined based on the MSE to retain low-level voxel information, as follows:

$$L_{\text{voxel}}(\hat{y}, y) = \frac{1}{D \times H \times W} \sum_{i=1}^D \sum_{j=1}^H \sum_{k=1}^W (\hat{y}_{ijk} - y_{ijk})^2, \quad (6)$$

where D , H , and W represent the depth, height, and width of the images, respectively, and i, j, k are the voxel indices along these dimensions.

Our final combined training objective L_{combined} is formulated as:

$$L_{\text{combined}} = L_{\text{voxel}} + L_{\text{SSIM}} + \lambda L_{\text{perc}}^{plane, \phi, j}, \quad (7)$$

where λ is a weighting factor for the cyclic 2.5D perceptual loss. The weights of L_{voxel} and L_{SSIM} are fixed to 1 to streamline the hyperparameter selection process.

3.4. Experiment

Training Details. An image translation model G is based on a 3D U-Net with a channel configuration of (64, 128, 256, 512, 1024) and utilizes instance normalization (Ulyanov et al.,

Algorithm 2: Setting Epochs for Plane Transitions

Require: Initial cycle duration for plane changes T ;
cycle duration scaling factor γ ;
maximum number of training epochs max_epoch ;
Ensure: Lists of epochs that change the selected plane in Algorithm 1 to axial ($axial_list$), coronal ($coronal_list$), and sagittal ($sagittal_list$)

```
 $axial\_list, coronal\_list, sagittal\_list = [], [], []$   
 $cnt = 0$   
while  $cnt < max\_epoch$  do  
  Append  $cnt$  to  $axial\_list$  ;  
  if  $(cnt + T) < max\_epoch$  then  
    Append  $cnt + T$  to  $coronal\_list$   
  end if  
  if  $(cnt + 2 \times T) < max\_epoch$  then  
    Append  $cnt + 2 \times T$  to  $sagittal\_list$   
  end if  
   $cnt \leftarrow cnt + 3 \times T$   
   $T \leftarrow \gamma \times T$   
end while  
return  $axial\_list, coronal\_list, sagittal\_list$ 
```

2016) in place of batch normalization (Ioffe and Szegedy, 2015). This model was employed in all primary experiments except for benchmarking. For the cyclic 2.5D perceptual loss, the initial cycle duration T was set to 120 to define the plane-switching frequency, with gradual adjustments controlled by the cycle duration scaling factor γ . The model training was conducted for up to 1000 epochs, with early stopping implemented to prevent overfitting and enhance experimental efficiency. The early stopping was triggered if the validation loss failed to improve over 30 consecutive epochs, starting after the completion of the second axial-coronal-sagittal cycle. The Adam optimizer (Kingma and Ba, 2015) was employed in conjunction with a cosine annealing scheduler (Loshchilov and Hutter, 2017), configured with a maximum learning rate of 5×10^{-4} . The cosine annealing period was aligned with the initial cycle duration T . Dropout (Srivastava et al., 2014) with a probability of 0.2 was applied as an additional measure to mitigate overfitting. Experiments were conducted using NVIDIA H100 (80GB VRAM) and NVIDIA RTX 6000 Ada (48GB VRAM). For experiments on the same topic, identical hardware setups were used to ensure consistency. The code is available at <https://github.com/labhai-dev/Cyclic-2.5D-Perceptual-Loss>.

Evaluation Metrics. To quantitatively evaluate the quality of the synthesized PET images, we employed the SSIM, peak signal-to-noise ratio (PSNR), and mean absolute error (MAE) as metrics. The analysis included both 3D average test values and 2D slice-wise evaluations for the SSIM, PSNR, and MAE. For the 2D slice-wise evaluations, assessments were conducted on axial, coronal, and sagittal slices, with results averaged across slices 20 to 90. The PSNR quantifies the signal-to-noise ratio relative to the peak intensity and is defined as follows:

$$\text{PSNR}(\hat{y}, y) = 10 \log_{10} \left(\frac{R^2}{\text{MSE}(\hat{y}, y)} \right) \quad (8)$$

where R is the maximum SUVR value of the ground truth PET image y . The MAE measures

| Cycle Duration Scaling Factor (γ) | SSIM(%) \uparrow | | | | PSNR(dB) \uparrow | | | |
|---|----------------------------------|----------------------------------|----------------------------------|----------------------------------|----------------------------------|----------------------------------|----------------------------------|----------------------------------|
| | Overall (3D) | Axial | Coronal | Sagittal | Overall (3D) | Axial | Coronal | Sagittal |
| Increase 2.0 ($\times 2.0$) | 90.47 \pm 3.66 | 86.96 \pm 4.38 | 86.79 \pm 4.36 | 85.51 \pm 4.80 | 29.12 \pm 3.07 | 30.36 \pm 4.52 | 27.91 \pm 2.99 | 28.22 \pm 3.09 |
| Increase 1.5 ($\times 1.5$) | 90.62 \pm 3.62 | 87.16 \pm 4.35 | 86.96 \pm 4.35 | 85.74 \pm 4.76 | 29.24 \pm 3.07 | 30.55\pm4.56 | 27.99 \pm 2.99 | 28.34 \pm 3.10 |
| Fixed ($\times 1.0$) | 90.61 \pm 3.62 | 87.16 \pm 4.32 | 86.95 \pm 4.33 | 85.74 \pm 4.76 | 29.20 \pm 3.04 | 30.54 \pm 4.61 | 27.96 \pm 2.96 | 28.32 \pm 3.07 |
| Decrease 1.5 ($\times 0.67$) | 90.64\pm3.61 | 87.22\pm4.32 | 87.03\pm4.33 | 85.74\pm4.76 | 29.24\pm3.12 | 30.51 \pm 4.58 | 28.02\pm3.06 | 28.36\pm3.10 |
| Decrease 2.0 ($\times 0.5$) | 90.51 \pm 3.69 | 87.02 \pm 4.40 | 86.83 \pm 4.42 | 85.59 \pm 4.83 | 29.09 \pm 3.03 | 30.34 \pm 4.52 | 27.88 \pm 2.98 | 28.21 \pm 3.07 |

Table 3: Grid search of the cycle duration scaling factor γ for the cyclic 2.5D perceptual loss. Performance was evaluated using the validation dataset. Experiments were carried out using increased, fixed, and decreased cycle durations. In all experiments, image translation was performed using a 3D U-Net model. The results are reported as mean \pm standard deviation. Reducing the cycle duration by a factor of 1.5 after each complete pass through all planes resulted in stable performance improvements across all planes, avoiding overfitting to any single plane. Note: Overall (3D) refers to the average 3D SSIM or PSNR, while Axial/Coronal/Sagittal corresponds to the average 2D SSIM or PSNR calculated for slices 20 to 90 in the axial, coronal, and sagittal planes, respectively.

the mean of absolute differences between the generated PET image \hat{y} and the ground truth PET image y , expressed as:

$$\text{MAE}(\hat{y}, y) = \frac{1}{N} \sum_{i=1}^N |\hat{y}_i - y_i|, \quad (9)$$

where N denotes the total number of voxels.

The SSIM was selected as the primary evaluation metric due to its ability to assess structural similarity, providing a more accurate representation of perceptual quality as perceived by the human visual system. Unlike metrics such as PSNR or MAE, which rely exclusively on pixel-level differences, SSIM evaluates the structural integrity of images. PSNR and MAE are particularly sensitive to pixel value discrepancies and can be significantly impacted by misregistration or noise introduced during the co-registration of MR and PET images. This sensitivity may result in skewed evaluations of image quality. Consequently, SSIM was deemed a more appropriate metric for assessing the performance of tau PET synthesis and was adopted as the primary evaluation criterion.

Cyclic 2.5D Perceptual Loss Hyperparameter Selection. We conducted hyperparameter selection for the cyclic 2.5D perceptual loss using the validation dataset. The primary focus of our initial experiment was to determine the optimal cycle duration scaling factor γ for switching between perceptual loss planes. Various strategies were explored, including increasing, fixing, and decreasing the intervals between cycles. As shown in Table 3, a grid search revealed that decreasing the duration of each subsequent cycle by a factor of 1.5 ($\times 0.67$) provided the most consistent optimization across both the overall plane and individual planes. Fixing the cycle duration scaling factor at 1.0 or increasing it by a factor of 1.5 showed a tendency toward overfitting, yielding strong performance only in specific planes. Based on these findings, the cycle duration scaling factor was set to decrease by 1.5 for all subsequent experiments. For fair evaluation, all these experiments utilized a perceptual loss model based on a VGG11 pre-trained on ImageNet-1K (Russakovsky et al., 2015), with feature maps extracted after the fourth ReLU layer. Additionally, the weight of the cyclic 2.5D perceptual loss (λ) was fixed at 1.0 throughout the experiments.

Experiments were subsequently performed to identify the optimal 2D pre-trained model ϕ and the perceptual loss weight λ for feature extraction in calculating the cyclic 2.5D

| Dataset | Perceptual Loss Model (ϕ) | Feature Extraction Layer (j) | n_{params} | Perceptual Loss Weight (λ) | SSIM(%) \uparrow | PSNR(dB) \uparrow | MAE \downarrow |
|-------------|----------------------------------|----------------------------------|---------------------|--------------------------------------|----------------------------------|----------------------------------|---------------------------------|
| RadImageNet | ResNet-50 | 3rd Block Stack | 8.53M | 1.0 | 90.37 \pm 3.58 | 29.02 \pm 3.10 | 10.05 \pm 4.85 |
| | InceptionNet v3 | 8th Inception Module | 8.97M | 0.5 | 90.48 \pm 3.67 | 29.11 \pm 3.19 | 10.03 \pm 4.79 |
| ImageNet-1K | ResNet-50 | 3rd Block Stack | 8.53M | 0.5 | 90.46 \pm 3.68 | 29.06 \pm 3.16 | 9.99 \pm 4.97 |
| | InceptionNet v3 | 8th Inception Module | 8.97M | 0.5 | 90.65 \pm 3.57 | 29.30 \pm 3.09 | 9.79 \pm 4.65 |
| | VGG-16 | 10th ReLU | 7.63M | 0.5 | 90.69\pm3.59 | 29.31\pm3.19 | 9.73\pm4.83 |

Table 4: Experimental results for selecting the cyclic 2.5D perceptual loss model ϕ and the cyclic 2.5D perceptual loss weight λ . Performance was evaluated on the validation set, comparing models pre-trained on the medical image dataset RadImageNet (Mei et al., 2022) and the natural image dataset ImageNet-1K (Russakovsky et al., 2015). The cyclic 2.5D perceptual loss weight λ was tested with values $\{0.1, 0.3, 0.5, 1, 3, 5\}$ for each model, and the configuration yielding the highest performance was reported. Feature extraction layers for each model were chosen so that the number of parameters remained comparable across all configurations. In all experiments, image translation was performed using a 3D U-Net model. The results are presented as mean \pm standard deviation. The best performance was achieved at the 23rd layer (10th ReLU) of the VGG16 pre-trained on ImageNet-1K, with a weight λ of 0.5. Note: The SSIM, PSNR, or MAE values represent performance across the 3D volume.

perceptual loss. The results are presented in Table 4. We employed models trained on medical image and natural image datasets to evaluate the feature extraction capabilities of models pre-trained on diverse domains. We utilized ResNet-50 (He et al., 2016) and Inception-v3 (Szegedy et al., 2016), both pre-trained on RadImageNet (Mei et al., 2022) for the medical domain. We employed models pre-trained on ImageNet-1K in the natural domain, including ResNet-50, Inception-v3, and VGG-16. The number of parameters from the input layer to the feature extraction layer was maintained at a comparable level across all models used for perceptual loss calculation to ensure a fair comparison. Among the tested models, the ImageNet-1K pre-trained VGG-16, configured to calculate perceptual loss at the 23rd layer (10th ReLU), achieved the highest performance on the validation set. Thus, this model was designated as the perceptual loss model ϕ , with the feature extraction layer j fixed at 23 and the cyclic 2.5D perceptual loss weight λ set to 0.5 for all subsequent experiments. For each experiment, the weight λ of the cyclic 2.5D perceptual loss was tested with values from $\{0.1, 0.5, 1, 3, 5\}$, and the configuration yielding the highest performance is reported. The complete results are provided in Suppl. A.1.

Benchmark. Quantitative evaluations and visual qualitative assessments were conducted to evaluate the performance of the proposed cyclic 2.5D perceptual loss for T1w MRI to tau PET translation. Comparative experiments were carried out by replacing the cyclic 2.5D perceptual loss component in the combined loss function with either the 2.5D or 3D perceptual loss. Additionally, the dataset generated using min-max normalization within the range of $(-1, 1)$ during the final PET normalization step was compared to assess the performance of the by-manufacturer standardization. The perceptual loss weight λ was set to 0.5 for all experiments. The perceptual loss model ϕ utilized the VGG-16 pre-trained on ImageNet-1K for both the 2.5D and cyclic 2.5D approaches, using the 10th ReLU layer as the feature extraction layer j . In contrast, the 3D approach employed the pre-trained ResNet-50 MedicalNet model (Chen et al., 2019) via `monai.losses.PerceptualLoss` from MONAI (version 1.3.2), with the feature extraction layer j set to the fourth block stack. A variety of generative approaches were employed for the 3D image translation model G , includ-

| Model | Perceptual Loss | SSIM(%) \uparrow | | | | PSNR(dB) \uparrow | | | |
|---------------------------|--------------------|----------------------------------|----------------------------------|----------------------------------|----------------------------------|----------------------------------|----------------------------------|----------------------------------|----------------------------------|
| | | Overall (3D) | Axial | Coronal | Sagittal | Overall (3D) | Axial | Coronal | Sagittal |
| PASTA w/ MRI only | None | 85.32 \pm 4.49 | 80.79 \pm 5.28 | 80.26 \pm 4.81 | 79.10 \pm 5.12 | 24.98 \pm 2.88 | 25.98 \pm 3.52 | 23.55 \pm 2.87 | 24.22 \pm 3.07 |
| ShareGAN w/ AD vs. MCI | None | 85.49 \pm 4.59 | 79.98 \pm 6.06 | 79.41 \pm 5.85 | 78.02 \pm 6.53 | 25.01 \pm 2.57 | 26.19 \pm 4.32 | 23.57 \pm 2.48 | 24.24 \pm 2.86 |
| U-Net | 3D | 87.18 \pm 5.47 | 82.23 \pm 6.71 | 82.12 \pm 7.03 | 80.89 \pm 7.62 | 25.51 \pm 1.99 | 25.01 \pm 1.80 | 24.48 \pm 2.12 | 24.44 \pm 2.16 |
| | 2.5D | 85.33 \pm 5.35 | 80.40 \pm 6.48 | 80.18 \pm 6.80 | 79.03 \pm 7.37 | 23.09 \pm 1.47 | 22.74 \pm 1.44 | 22.55 \pm 1.66 | 22.52 \pm 1.70 |
| | Cyclic 2.5D (Ours) | 88.03\pm5.89 | 82.78\pm7.59 | 82.75\pm7.59 | 81.49\pm8.26 | 26.71\pm2.81 | 26.56\pm2.68 | 25.32\pm2.83 | 25.48\pm2.87 |
| U-Net \dagger | 3D | 89.81 \pm 3.69 | 85.83 \pm 4.44 | 85.82 \pm 4.40 | 84.60 \pm 4.70 | 28.34 \pm 2.65 | 29.17 \pm 3.71 | 27.09 \pm 2.53 | 27.49 \pm 2.79 |
| | 2.5D | 90.01 \pm 3.49 | 86.02 \pm 4.27 | 86.05 \pm 4.20 | 84.91 \pm 4.48 | 28.33 \pm 2.65 | 29.26 \pm 3.83 | 27.06 \pm 2.55 | 27.52 \pm 2.83 |
| | Cyclic 2.5D (Ours) | 90.36\pm3.59 | 86.55\pm4.31 | 86.58\pm4.22 | 85.40\pm4.51 | 28.79\pm2.58 | 29.60\pm3.68 | 27.52\pm2.43 | 27.93\pm2.72 |
| UNETR \dagger | 3D | 89.68 \pm 3.74 | 85.80 \pm 4.44 | 85.80 \pm 4.36 | 84.54 \pm 4.70 | 28.25 \pm 2.39 | 28.82 \pm 3.24 | 27.16\pm2.20 | 27.41 \pm 2.46 |
| | 2.5D | 89.68 \pm 3.64 | 85.77 \pm 4.28 | 85.76 \pm 4.19 | 84.58 \pm 4.47 | 28.34\pm2.27 | 29.16 \pm 3.36 | 27.11 \pm 2.02 | 27.57\pm2.42 |
| | Cyclic 2.5D (Ours) | 89.93\pm3.27 | 86.03\pm3.92 | 86.07\pm3.89 | 84.84\pm4.18 | 28.34 \pm 2.51 | 29.32\pm3.65 | 27.13 \pm 2.29 | 27.57 \pm 2.63 |
| SwinUNETR \dagger | 3D | 90.20 \pm 3.68 | 86.42 \pm 4.44 | 86.45 \pm 4.29 | 85.26 \pm 4.64 | 28.28 \pm 2.64 | 29.08 \pm 3.72 | 27.12 \pm 2.38 | 27.46 \pm 2.76 |
| | 2.5D | 90.23 \pm 3.55 | 86.42 \pm 4.35 | 86.51 \pm 4.19 | 85.30 \pm 4.53 | 28.60\pm2.58 | 29.47 \pm 3.61 | 27.37 \pm 2.41 | 27.86\pm2.72 |
| | Cyclic 2.5D (Ours) | 90.29\pm3.40 | 86.57\pm4.11 | 86.69\pm4.01 | 85.36\pm4.38 | 28.52 \pm 2.59 | 29.47\pm3.59 | 27.41\pm2.35 | 27.72 \pm 2.71 |
| CycleGAN \dagger | None | 84.69 \pm 4.81 | 79.19 \pm 5.58 | 78.49 \pm 5.40 | 76.94 \pm 5.75 | 26.12 \pm 2.39 | 26.70 \pm 3.16 | 24.75 \pm 2.22 | 25.25 \pm 2.51 |
| | 3D | 85.63 \pm 5.03 | 80.58 \pm 5.67 | 79.84 \pm 5.65 | 78.39 \pm 5.98 | 26.34 \pm 2.38 | 26.87 \pm 3.17 | 24.99 \pm 2.20 | 25.45 \pm 2.55 |
| | 2.5D | 87.15 \pm 4.32 | 82.28 \pm 5.01 | 82.16 \pm 4.89 | 80.75 \pm 5.14 | 27.18\pm2.45 | 27.71\pm3.26 | 25.91\pm2.24 | 26.27\pm2.51 |
| | Cyclic 2.5D (Ours) | 87.69\pm3.97 | 82.82\pm4.78 | 82.78\pm4.62 | 81.27\pm4.95 | 27.16 \pm 2.32 | 27.62 \pm 3.21 | 25.90 \pm 2.19 | 26.24 \pm 2.43 |
| Pix2Pix \dagger | None | 82.69 \pm 4.39 | 76.73 \pm 5.05 | 76.35 \pm 4.83 | 74.56 \pm 5.20 | 26.48 \pm 2.01 | 26.56 \pm 2.48 | 25.14 \pm 1.82 | 25.40 \pm 2.06 |
| | 3D | 84.10 \pm 4.72 | 78.02 \pm 5.30 | 77.82 \pm 5.11 | 75.90 \pm 5.49 | 26.47 \pm 2.14 | 26.48 \pm 2.62 | 25.12 \pm 1.90 | 25.35 \pm 2.20 |
| | 2.5D | 86.66 \pm 4.08 | 81.41 \pm 4.74 | 81.45 \pm 4.54 | 79.72 \pm 4.85 | 27.06 \pm 2.12 | 27.41 \pm 2.90 | 25.74 \pm 1.95 | 26.02 \pm 2.23 |
| | Cyclic 2.5D (Ours) | 87.63\pm3.91 | 82.65\pm4.63 | 82.67\pm4.45 | 81.08\pm4.74 | 27.55\pm2.21 | 28.18\pm3.24 | 26.25\pm1.99 | 26.66\pm2.34 |

Table 5: Quantitative comparisons of various combined loss functions and original losses (None) in tau PET synthesis tasks. Evaluations were performed across multiple models and on test datasets that were preprocessed using different methods. Models trained using the proposed cyclic 2.5D perceptual loss combined with the by-manufacturer tau PET SUVR standardization demonstrated superior performance compared to other approaches. The combined loss functions include perceptual loss, SSIM loss (L_{SSIM}), and MSE loss (L_{voxel}). The results reported as mean \pm standard deviation. The dagger symbol (\dagger) indicates models trained on datasets preprocessed using the proposed by-manufacturer standardization of tau PET SUVR, and models without this symbol were trained on datasets preprocessed with min-max normalization. Note: Overall (3D) refers to the average 3D SSIM or PSNR, while Axial/Coronal/Sagittal corresponds to the average 2D SSIM or PSNR calculated for slices 20 to 90 in the axial, coronal, and sagittal planes, respectively.

ing the 3D U-Net, U-Net-like models (UNETR and SwinUNETR), and GAN-based models (CycleGAN and Pix2Pix), with the 3D U-Net serving as the generator in the GAN-based models. The experiments involving the 3D U-Net and its variants employed the combined loss function described in Equation (7). Two distinct loss configurations were evaluated for the CycleGAN and Pix2Pix experiments: the original loss and a combination of the original loss with the proposed combined loss. CycleGAN’s original loss consists of adversarial loss, cycle consistency loss, and identity loss. Pix2Pix’s original loss comprises adversarial loss and L1 loss. The proposed loss was incorporated into CycleGAN’s original loss to create a combined loss configuration, whereas for Pix2Pix, the L1 loss was substituted with the proposed loss. Since experiments involving the 2.5D and 3D perceptual loss models did not require delayed early stopping, early stopping was applied after completing the first cycle of the cosine annealing scheduler across all experiments. The maximum learning rate was set to $2e-4$ for the CycleGAN and Pix2Pix experiments.

Quantitative comparisons were conducted with the state-of-the-art algorithms designed for synthesizing PET images from MR images to further validate the effectiveness of the proposed approach. Specifically, the open-source implementations of PASTA (Li et al., 2024)

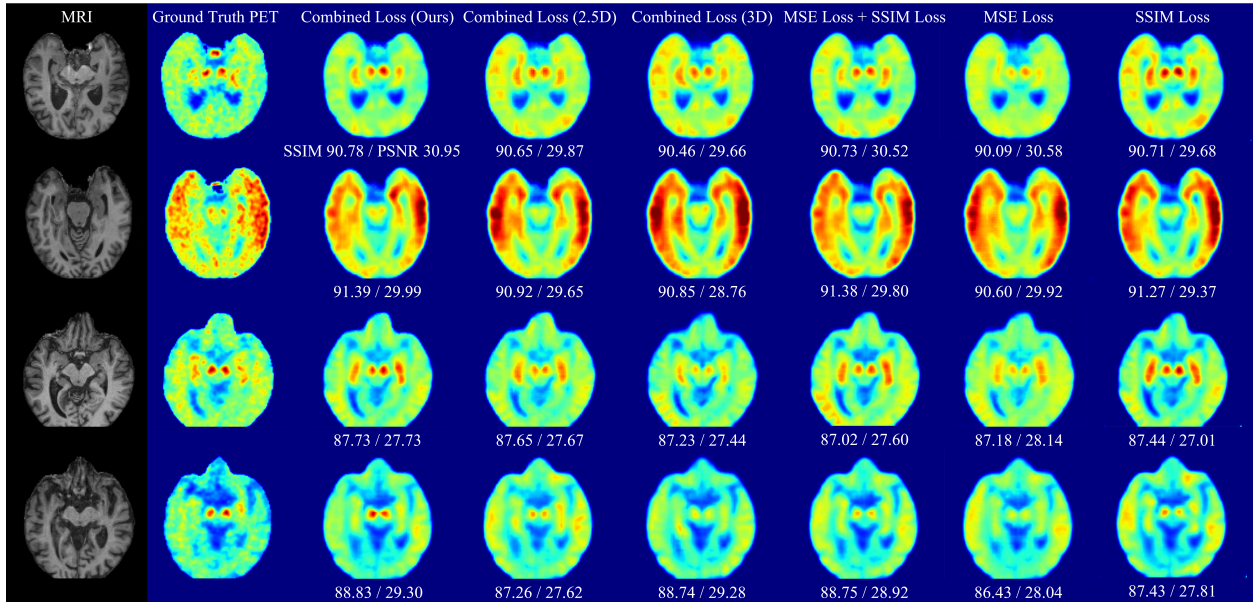


Figure 4: Qualitative comparison of images generated by the 3D U-Net with different loss functions. Our method (the third column) demonstrates superior accuracy in capturing tau burden compared to other methods, clearly illustrating hyperphosphorylated tau deposition. The first column presents the input T1w MR images, the second illustrates the ground truth tau PET images, and the subsequent columns show the generated tau PET images. The SSIM and PSNR values between the ground truth tau PET image and the generated tau PET image are reported from the third column to the final column. Note: The SSIM or PSNR values represent performance across the 3D volume.

and ShareGAN with joint learning (Wang et al., 2024) were utilized. We employed our own dataset and preprocessing pipeline due to the unavailability of the datasets and preprocessing scripts used in their experiments—apart from the training algorithms. The MR and PET images were preprocessed according to the steps outlined in Section 3.2, excluding resizing and normalization. Subsequently, the image pairs were resized and normalized to match the input requirements of each framework. Specifically, PASTA utilized the MRI and PET pairs normalized to the range (0, 1) with dimensions (128×128×128), whereas ShareGAN applied normalization to the range (-1, 1) with dimensions (256×256×256). Patient metadata beyond the MR and PET images was excluded during training with PASTA to ensure a fair comparison. For ShareGAN, joint learning was performed via a binary classification task to distinguish AD from EMCI/MCI/LMCI.

Regional of Interest (ROI) Analysis An ROI analysis was performed after the quantitative and visual qualitative analysis to demonstrate the effectiveness of the proposed method in capturing tau PET brain signatures in Alzheimer’s patients. The proposed method, which utilizes the combined loss incorporating the cyclic 2.5D perceptual loss, was compared to the models trained by replacing the cyclic 2.5D perceptual loss with either the 3D or 2.5D loss. All PET scans, including the ground truth PET images and those generated by the aforementioned models, were registered to a standard anatomical space defined by the fsaverage template provided by **FreeSurfer**. Specifically, the MR images were first registered to the fsaverage surface, and the linear transformation matrix obtained during this registration was subsequently applied to align the corresponding PET images to the fsaverage surface. Since

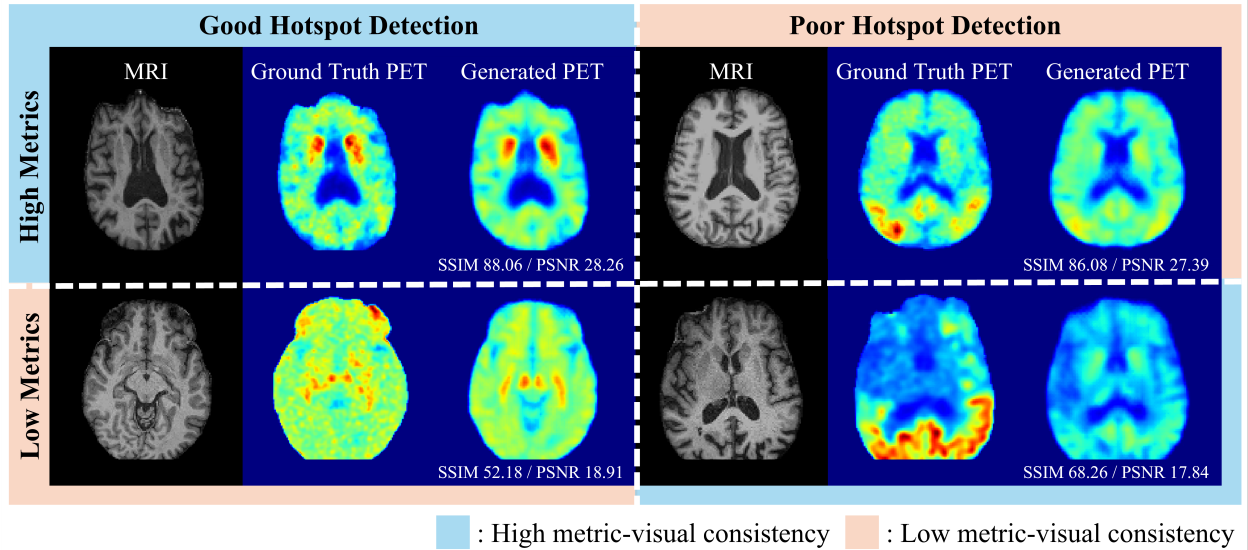


Figure 5: Visualization of multiple pairs comprising an input MR image, the corresponding ground truth tau PET image, and the generated tau PET image. The top-left and bottom-right pairs demonstrate a consistent alignment between the quantitative metrics and the detection of visual hot spots, defined as regions with high SUVR values in the ground truth tau PET images. However, the top-right and bottom-left pairs indicate cases where the metrics did not adequately reflect the visual hot spot detection. Note: The SSIM or PSNR values are calculated for individual 2D axial slices.

the MR and PET images were co-registered in the MRI space, voxel-wise correspondence of the atlas-aligned PET data across subjects was ensured. ROIs were defined based on the Desikan-Killiany atlas provided by `FreeSurfer`. The SUVR values within each region, as defined by the atlas-based ROI segmentation map, were averaged to derive a representative PET SUVR for each region to extract region-specific PET signals. The mean SUVR for each ROI was calculated using the following formula:

$$\mu_{\text{ROI}} = \frac{1}{N_{\text{ROI}}} \sum_{i=1}^{N_{\text{ROI}}} I(v_i), \quad (10)$$

where μ_{ROI} represents the mean SUVR for a specific ROI, N_{ROI} denotes the total number of voxels within the ROI, and $I(v_i)$ indicates the SUVR value of the i -th voxel within the ROI. The ROI analysis was conducted by calculating the MSE for each cortical region defined in the Desikan-Killiany atlas. This process involved comparing the mean SUVR from the ground truth PET images with the mean SUVR from the generated PET images across different settings. The analysis was performed for all 78 subjects in the test dataset, and the results were averaged to compute the overall MSE for each ROI across all experimental conditions. Specifically, the MSE for a given ROI, denoted as MSE_{ROI} , was calculated as follows:

$$\text{MSE}_{\text{ROI}} = \frac{1}{N_{\text{subject}}} \sum_{i=1}^{N_{\text{subject}}} (\hat{\mu}_{\text{ROI},i} - \mu_{\text{ROI},i})^2, \quad (11)$$

where N_{subject} represents the total number of test subjects, $\hat{\mu}_{\text{ROI},i}$ denotes the mean SUVR

of the generated PET image for the specified ROI of the i -th subject, and $\mu_{ROI,i}$ corresponds to the mean SUVR of the ground truth PET image for the same ROI and subject.

4. Results

4.1. Benchmark Evaluation

Quantitative comparison Table 5 presents the quantitative results, demonstrating that the proposed cyclic 2.5D perceptual loss outperformed other methods across most evaluation metrics. Specifically, the SSIM values achieved by the proposed method consistently exceeded those of all comparative approaches across all models, evaluated at both the whole-volume (3D) level and the per-plane (2D) level. The combined loss function incorporating the cyclic 2.5D perceptual loss exhibited superior performance under equivalent conditions compared to the two state-of-the-art open-source frameworks for synthesizing PET from MRI: the PASTA and the ShareGAN with joint learning. Furthermore, the cyclic 2.5D perceptual loss achieved better results across various generative models compared to the 3D and 2.5D perceptual losses. The preprocessing method that standardizes PET SUVR values according to manufacturer outperformed the min-max normalization approach, which merely rescales SUVR values to a predetermined range. Comprehensive experimental results, including MAE metrics, are provided in Suppl. A.2.

Qualitative comparison The proposed method also produced qualitatively superior results, accurately capturing pathological tau accumulation and NFT distributions. Figure 4 illustrates the axial slices of PET images generated by the models trained with various configurations of the combined loss, including the cyclic 2.5D, 3D, and 2.5D perceptual losses. Among these configurations, the model trained with the cyclic 2.5D perceptual loss demonstrated the highest precision in identifying tau tangle hot spots while minimizing the misidentification of neuropathologically spared regions. However, some inconsistencies were observed in certain samples between the SSIM and PSNR values and the visual quality of the generated PET images. These discrepancies are visualized in Figure 5, which presents axial-side comparisons.

4.2. ROI Analysis

ROI analysis demonstrated that the model trained using the proposed cyclic 2.5D perceptual loss generated values closer to the actual PET in Alzheimer’s tau pathology regions compared to the conventional 2.5D and 3D methods. The primary cortical areas where tau tangles accumulate the most were identified and performance was compared in the top 20 (and 10) regions (Figure 6). Comprehensive ROI analysis results are provided in Suppl. A.3. The areas were identified based on the mean PET SUVR averaged among the study participants. The MSE_{ROI} between the generated PET and the actual PET was lower in 17 out of the 20 ROIs when using the cyclic 2.5D perceptual loss, compared with the 2.5D or 3D approaches. In the banks of the superior temporal sulcus, cyclic 2.5D achieved MSE of 0.59 in the left hemisphere (lh) and 0.40 in the right hemisphere (rh), reducing MSE by 18.72% (lh) and 18.56% (rh) compared to the conventional 2.5D method, and by 17.99% (lh) and 8.39% (rh) compared to the 3D method. In the entorhinal cortex, cyclic 2.5D reduced MSE by 16.75% (lh)/22.90% (rh) compared with 2.5D and 11.94% (lh)/13.72% (rh) compared with 3D. Cyclic 2.5D reduced MSE by 10.31% (lh)/10.74% (rh) compared to 2.5D and

MSE Relative to GT PET in Primary Alzheimer’s Tau Pathology Areas in the Cortex

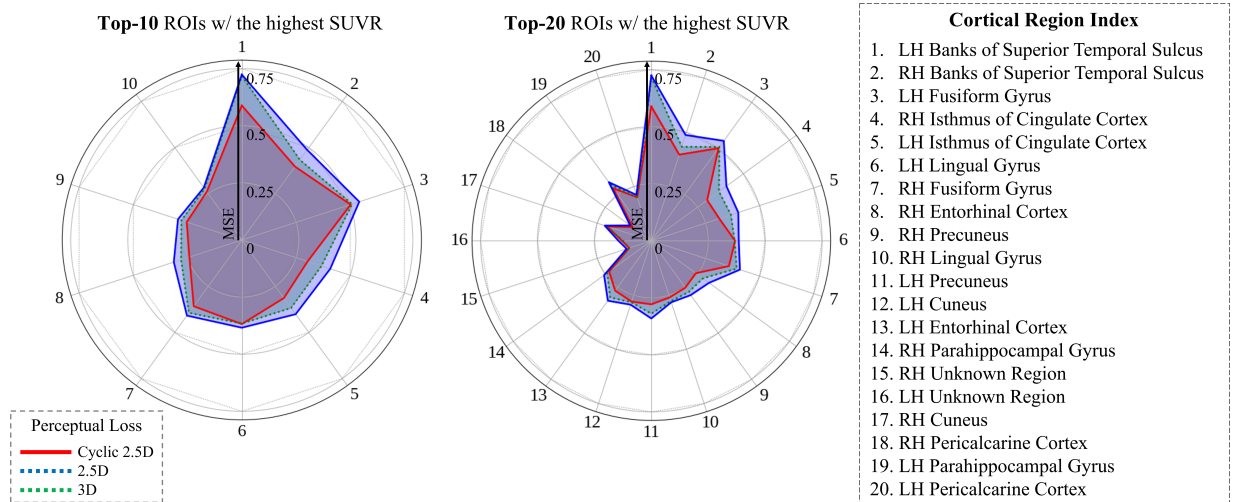


Figure 6: Prediction performance (MSE) of tau PET synthesis across key cortical regions associated with AD pathology. Analysis was performed by calculating MSE between the mean SUVR of the actual tau PET and the mean SUVR of the generated tau PET for each cortical region. The results are stratified based on the ground truth tau PET SUVR mean across the study participants: the top 10 regions with the highest mean SUVR are displayed on the left, and the top 20 regions are shown on the right. The proposed cyclic 2.5D perceptual loss exhibited superior performance by generating signals that most closely resembled the original tau PET images. Specifically, it achieved lower MSE values in 9 out of the top 10 regions and 17 out of the top 20 regions, compared to both the standard 2.5D and 3D perceptual losses.

6.63% (lh)/4.46% (rh) compared to 3D in the parahippocampal gyrus. Other primary tau pathology areas showing MSE reduction are the isthmus cingulate, precuneus, and fusiform gyrus.

4.3. Ablation Study

We conducted ablation studies to evaluate the effectiveness of each component comprising the proposed combined loss function. Our method, which employs a combined loss integrating $L_{perc}^{plane,\phi,j}$, L_{voxel} and L_{SSIM} , outperformed both the individual and combined configurations of L_{voxel} and L_{SSIM} . The results presented in Table 6 confirm the effectiveness of the proposed combined loss function. Specifically, we tested with L_{voxel} only, L_{SSIM} only, combined L_{voxel} and L_{SSIM} , combined L_{voxel} and $L_{perc}^{plane,\phi,j}$, and combined L_{SSIM} and $L_{perc}^{plane,\phi,j}$, to examine performance variations associated with each component within the combined loss $L_{combined}$. Additionally, we conducted further ablation studies to verify the impact of each step in our preprocessing pipeline. The results are provided in Suppl. A.4.

5. Discussion

This study holds significant value by demonstrating the potential for synthesizing tau PET imaging, an established biomarker for AD pathology, from structural imaging data, specifically T1w MRI. Despite its proven value, the clinical application of tau PET remains limited due to high costs, invasiveness, and restricted availability, particularly in primary

| Loss Function | SSIM(%) \uparrow | PSNR(dB) \uparrow | MAE \downarrow |
|--|----------------------------------|----------------------------------|---------------------------------|
| L_{voxel} | 89.37 \pm 3.61 | 28.50 \pm 2.64 | 10.37 \pm 3.80 |
| L_{SSIM} | 90.26 \pm 3.68 | 28.27 \pm 2.47 | 9.93 \pm 4.12 |
| $L_{\text{voxel}} + L_{SSIM}$ | 90.32 \pm 3.59 | 28.51 \pm 2.76 | 9.75 \pm 4.09 |
| $L_{\text{voxel}} + L_{\text{perc}}^{\text{plane},\phi,j}$ | 89.77 \pm 3.38 | 28.57 \pm 2.60 | 9.80 \pm 3.74 |
| $L_{SSIM} + L_{\text{perc}}^{\text{plane},\phi,j}$ | 90.31 \pm 3.62 | 28.47 \pm 2.59 | 9.50 \pm 4.17 |
| $L_{\text{voxel}} + L_{SSIM} + L_{\text{perc}}^{\text{plane},\phi,j}$ (Ours) | 90.36\pm3.59 | 28.79\pm2.58 | 9.26\pm4.00 |

Table 6: Ablation study of the components of the proposed combined loss function. The experiments were conducted using a 3D U-Net on a test dataset preprocessed with our method. The results are reported as mean \pm standard deviation. Note: The SSIM, PSNR, or MAE results represent the entire 3D volume.

care and general neurology settings. The proposed MRI-based synthesis method has the potential to address these limitations by facilitating broader clinical and research utility through a non-invasive, cost-effective surrogate measure of tau pathology. A key clinical application of this surrogate measure is its potential use as a pre-screening or triage tool before referring patients to specialized centers. The synthesized PET could help stratify patients according to their likelihood of harboring significant AD-related pathology by providing a non-invasive approximation of tau burden. For example, MRI-based tau prediction could help identify patients with a high likelihood of significant tau pathology in memory clinics or general neurology settings where MRI is routinely performed during cognitive evaluations. Individuals with high predicted tau burden may then be prioritized for confirmatory testing (e.g., tau PET or cerebrospinal fluid analysis) or referral to tertiary care, whereas those with low predicted burden could be managed locally or monitored over time. This proposed workflow aligns with emerging strategies in AD care, which advocate for the use of less invasive, more accessible biomarkers to reduce the number of patients undergoing costly confirmatory tests (Jack Jr et al., 2020). Just as inexpensive blood-based biomarkers are being integrated into primary care workflows to expedite diagnosis and facilitate earlier therapeutic intervention (Pleen et al., 2024), a synthesized tau measure from MRI could serve a similar triage function within the imaging domain. By identifying individuals with probable AD pathology prior to PET imaging, clinicians can make more informed decisions about which patients truly require advanced imaging. This stratified approach is particularly valuable in the current era of newly available disease-modifying therapies, such as monoclonal antibodies (Van Dyck et al., 2023; Cummings et al., 2024), for which confirmation of tau pathology is a prerequisite for treatment eligibility. However, given the high cost, limited availability, and logistical challenges associated with tau PET, it remains impractical to perform PET scans on all potentially eligible patients (Lee et al., 2024). Therefore, MRI-based tau estimation could serve as a scalable, non-invasive method for guiding therapeutic decision-making across diverse clinical and research populations.

The established temporal and spatial dynamics of molecular pathology and neurodegeneration in AD support the feasibility of predicting tau PET from structural MRI. According to the widely accepted AD biomarker cascades (Jack et al., 2010; Guo et al., 2021), molecular alterations precede structural brain changes during disease progression. Amyloid- β accumulation typically initiates this cascade, often occurring decades before clinical symptom onset, followed by changes in soluble tau. Subsequently, tau PET becomes positive, and

only then do we observe widespread neurodegeneration and brain atrophy detectable via MRI. In this sequence, tau NFT accumulation begins when individuals are still minimally impaired, ultimately giving rise to the neurodegenerative changes that structural MRI can detect. Neuropathological evidence from Braak and Braak (1991); Braak et al. (2006) aligns with this progression. In the earliest Braak stages (I–II), tau pathology is restricted to the entorhinal cortex and adjacent regions, without detectable atrophy or clinical symptoms. As the disease advances to Braak stages III–IV, tangles spread to limbic structures and finally to neocortical regions in stages V–VI, coinciding with the emergence and progression of cognitive impairment. By the time patients reach the stage of MCI or early dementia, there is already substantial tau deposition in limbic and neocortical areas, accompanied by measurable tissue loss in those same regions. This well-defined pathological trajectory implies that structural MRI may capture latent neurodegenerative patterns reflecting underlying tau pathology, supporting the hypothesis that MRI-based features could reliably predict tau PET findings. Importantly, in our study, all MRI–PET scan pairs were acquired within a one-year interval, minimizing the potential impact of disease progression between scans. This temporal proximity ensures that the structural and molecular imaging data represent comparable stages of the disease, thereby strengthening the validity of our predictive modeling approach.

Our proposed method exhibits quantitatively superior performance compared to the two publicly available approaches for synthesizing PET images from MRI. The proposed cyclic 2.5D perceptual loss mostly outperforms the 2.5D and 3D perceptual losses in the 3D U-Net, its variants, and the GAN-based models. This suggests that the cyclic 2.5D perceptual loss can be effectively utilized not only in U-Net-based architectures but also in other image synthesis frameworks and training algorithms, including adversarial training. During training, the cyclic 2.5D perceptual loss operates by periodically switching the retrieval plane for single-plane 2D perceptual loss calculations. This periodic switching enables consistent optimization across the three planes, ensuring excellent performance in both 3D metrics and all three planar 2D metrics. Conceptually, this process is akin to shaping a clay cube by alternately patting each side, ensuring balanced refinement. While initial changes in the retrieval plane may lead to transient spikes in validation loss, these diminish over time as the model adapts. By treating all planes equivalently over the same number of epochs, the cyclic strategy mitigates overfitting—a common limitation of traditional 2.5D perceptual loss, which aggregates plane-wise losses and risks overemphasizing “easier” planes. The continuous alternation of the retrieval plane further enhances robustness by avoiding excessive reliance on any single plane. This strategy is analogous to the cyclic learning rate approach (Smith, 2017), which enables models to explore broader parameter space and escape saddle points by cyclically varying the learning rate. Similarly, in the cyclic 2.5D perceptual loss, the model undergoes high-learning-rate-like adjustments immediately following a plane change, optimizing perceptual quality on the new plane while fine-tuning during subsequent epochs. As the cycle interval shortens, the model performs increasingly finer adjustments across all planes, ultimately achieving a more balanced and optimized synthesis. The cyclic 2.5D perceptual loss enhances the fidelity and diagnostic utility of synthesized images by ensuring comprehensive optimization across all planes while mitigating reliance on dominant anatomical perspectives. This approach bolsters the robustness and generalizability of synthetic imaging, thereby potentially enhancing its applicability in clinical decision-making

and medical research.

In the UNETR, the SwinUNETR, and the CycleGAN, the cyclic 2.5D perceptual loss yields in lower PSNR values compared to the 2.5D and 3D perceptual losses for certain planes or full (3D) view. As transformer-CNN hybrid models, the UNETR and the SwinUNETR utilize transformer (Vaswani et al., 2017) encoders to learn patch-wise feature representations. Since the cyclic 2.5D perceptual loss evaluates feature similarity independently across different planes, it may not align optimally with the global feature aggregation mechanism inherent to transformer-based architectures. This potential misalignment could hinder the transformer’s ability to integrate contextual information across 3D space, thereby resulting in suboptimal pixel-wise precision (as measured by PSNR) compared to conventional perceptual losses. In the case of the CycleGAN, which employs an unpaired image-to-image translation framework requiring bidirectional modality transformation, the training process involves two generators and two discriminators operating in an adversarial setting. Maintaining cycle consistency is crucial for optimizing the CycleGAN. Since the cyclic 2.5D perceptual loss assesses perceptual similarity independently for each plane, it may conflict with the CycleGAN’s requirement to preserve 3D spatial consistency. However, it is important to note that while higher PSNR values generally indicate lower pixel-wise discrepancies, they do not necessarily guarantee the preservation of structural or pathological features. Notably, our method outperforms all comparison methods in terms of SSIM, the primary metric for T1w MRI to tau PET translation, indicating superior perceptual fidelity in the synthesized images.

Standardizing tau PET SUVR values based on scanner manufacturers improved quantitative performance compared to min-max normalization. This improvement is likely due to the inherent consistency of PET images produced by the same manufacturer, particularly in regions with elevated SUVR values that are relevant to AD. Conversely, SUVR distributions exhibit statistical variability across different manufacturers. Min-max normalization rescales all PET images to a fixed range, disregarding these manufacturer-specific SUVR characteristics. As a result, it may attenuate or fail to preserve high-SUVR regions that are pathophysiologically critical for AD assessment. By implementing manufacturer-specific standardization of PET SUVR, our method minimizes performance degradation caused by discrepancies in SUVR distributions across manufacturers. This method not only preserves clinically significant uptake patterns but also yields demonstrable improvements in quantitative performance, as validated through comprehensive evaluations. By minimizing scanner-induced heterogeneity, our approach ensures that SUVR values remain biologically meaningful and comparable across datasets, ultimately improving the robustness and reliability of quantitative analyses in synthesized tau PET.

Most importantly, our training pipeline synthesizes PET images that more accurately preserve regional tau pathology than compared to those generated using the conventional 2.5D and 3D perceptual losses. The ROI analysis revealed that the PET images generated by our method exhibited the highest fidelity to the original PET images, particularly in clinically significant regions with prevalent tau pathology. This advantage was most pronounced in regions severely affected by tau deposition, which aligns with the areas delineated by Braak staging (Braak and Braak, 1991; Braak et al., 2006). The strongest PET signal was observed in the banks of the superior temporal sulcus, consistent with prior studies reporting early elevations in tau PET uptake in this region (Insel et al., 2020). Our method exhibited

enhanced performance in this region, further demonstrating its capability to more accurately represent regional tau burden. Similar improvements were noted in the entorhinal cortex, the initial site of tau tangle formation corresponding to Braak stages I-II (Van Hoesen et al., 1991; Igarashi, 2023), and in the parahippocampal gyrus, which is associated with early AD and MCI pathology spanning Braak stages I-IV (Mitchell et al., 2002). The isthmus cingulate, increasingly affected during Braak stages III-IV (Maass et al., 2017), and the fusiform gyrus, linked to cognitive deficits in AD and corresponding to Braak stages III-IV (Seemiller et al., 2021; Lowe et al., 2018), also demonstrated improvements. Furthermore, enhanced performance was observed in the precuneus, a region prominently affected in advanced Braak stages V-VI (Chen et al., 2021; Pascoal et al., 2021). These findings emphasize the capability of the cyclic 2.5D method to accurately capture tau pathology across brain regions encompassing a wide range of Braak stages, from early (I-II) to advanced (V-VI). Crucially, strong SUVR signals were detected in regions typically associated with early Alzheimer’s pathology, aligning with the ADNI cohort’s characteristics, which predominantly includes individuals in the prodromal or early symptomatic stages of AD. Additionally, the qualitative visual analysis confirmed that our approach more effectively represents the spatial and pathological characteristics of tau accumulation. These are essential for accurately modeling the progressive stages of tau-related neuropathology in AD. The proposed method achieved qualitatively superior performance, demonstrating its ability to capture and reflect tau pathology with greater accuracy compared to the existing methods. These results suggest that the cyclic 2.5D approach enables generative models to learn better mappings that retain tau-related pathological information than those trained with traditional perceptual loss configurations. This enhanced capability emphasizes the superiority of our plane-wise cyclic 2.5D perceptual loss in preserving critical pathological information, particularly in the context of AD-related neurodegenerative disorders. Consequently, this approach not only improves the precision of pathological staging in AD but also enhances the reliability of tau PET synthesis, making it highly suitable for a range of clinical applications, including disease progression monitoring or therapeutic response assessment.

Several images with high PSNR or SSIM values exhibited poor visual quality, particularly in PET images with predominantly low SUVR values interspersed with a few prominent tau hot spots. This observation emphasizes the inherent limitations of relying solely on SSIM or PSNR for evaluating tau PET imputation tasks and suggests the necessity of region-specific analyses that consider variations across different brain areas. This problem is particularly significant given that the primary objective of tau PET imaging is to identify the pathological localization of NFTs in the brain. The failure to detect hot spots compromises the clinical utility of synthesized tau PET images, emphasizing the need for an evaluation metric that addresses these shortcomings. Therefore, developing an evaluation metric that effectively accounts for these challenges is essential.

Despite its advantages, the cyclic 2.5D perceptual loss also has certain limitations. It requires many epochs due to the current configuration, which activates early stopping in later stages. However, premature termination of training in earlier stages significantly increases the risk of overfitting to a single plane, mainly due to the large number of epochs within the initial cycle durations. Additionally, the method considers all slices, including those with minimal or irrelevant anatomical information. Many peripheral slices contain negligible tissue, where more straightforward metrics such as MSE and SSIM are sufficient. Future

work should address these issues to maximize the benefits of perceptual loss while reducing computational costs. Furthermore, the development of a robust evaluation metric tailored for PET image synthesis is imperative, as traditional metrics often fail to accurately capture the true visual quality and clinical relevance of the generated images.

6. Conclusion

We introduce a cyclic 2.5D perceptual loss function and combine it with SSIM and MSE losses to effectively synthesize 3D tau PET images from 3D T1w MRI inputs. The proposed loss function captures perceptual information across all imaging planes while mitigating the risk of overfitting to specific planes. Furthermore, we introduce a by-manufacturer PET SUVR standardization approach to address the variability of SUVR distributions arising from tau PET images acquired using different scanners. Extensive evaluations conducted with paired 3D T1w MRI and tau PET images from the ADNI database validate the effectiveness and versatility of our proposed method across various generative modeling frameworks. Quantitative analyses demonstrate that our approach outperforms traditional 2.5D and 3D perceptual losses, as well as current state-of-the-art techniques, in producing high-quality synthesized tau PET images. Qualitatively, our method achieves superior accuracy in detecting tau aggregate hot spots compared to existing approaches. ROI analyses further confirm that synthesized images generated by our method closely resemble actual tau PET images, particularly in clinically significant regions associated with tau pathology, surpassing results obtained using conventional perceptual losses. Future research should focus on refining the cyclic 2.5D perceptual loss by selectively prioritizing slices that contain significant anatomical information and developing novel evaluation metrics specifically tailored to PET image synthesis tasks. This approach holds potential as a noninvasive tau biomarker that could serve as a pre-screening or classification tool in both research and clinical settings, supporting broader applications of tau-related assessments without introducing additional risks or costs to patients. Ultimately, by facilitating the generation of accurate, high-quality tau PET images from structural MRI, our approach holds substantial promise for improving the diagnosis and management of AD and MCI through precise identification of neuroanatomical regions with significant neurofibrillary tangle accumulation.

CRedit authorship contribution statement

Moon, J.: Formal Analysis, Investigation, Software, Validation, Visualization, Writing – Review & Editing. **Kim, S.:** Methodology, Data curation, Formal Analysis, Investigation, Software, Visualization, Writing – original draft, Writing – Review & Editing. **Chung, H.:** Funding acquisition, Resources, Writing – Review & Editing. **Jang, I.:** Conceptualization, Methodology, Formal Analysis, Funding acquisition, Resources, Supervision, Writing – Review & Editing.

Declaration of generative AI and AI-assisted technologies in the writing process

During the preparation of this work the authors used ChatGPT in order to enhance the readability and language of the manuscript. After using this tool, the authors reviewed and edited the content as needed and take full responsibility for the content of the publication.

Acknowledgements

The authors appreciate Chanik Kang, Daehwan Kim, and Jiwoong Yang for providing valuable feedback during the manuscript preparation. This work was supported by the National Institute of Health (NIH) research projects (2024ER040700, 2025ER040300), the National Supercomputing Center with supercomputing resources including technical support (KSC-2024-CRE-0021, KSC-2025-CRE-0065), the National Research Foundation of Korea (NRF) grants funded by the Korean government (MSIT), (RS-2024-00455720, RS-2024-00338048, RS-2024-00414119), a grant of the Korea Health Technology R&D Project through the Korea Health Industry Development Institute (KHIDI), funded by the Ministry of Health & Welfare (RS-2025-02220534), and Hankuk University of Foreign Studies Research Fund of 2025. The work was also supported by the Republic of Korea's MSIT, under the Global Research Support Program in the Digital Field program (RS-2024-00412644) supervised by the IITP (Institute of Information and Communications Technology Planning & Evaluation), Culture, Sports and Tourism R&D Program through the Korea Creative Content Agency grant funded by the Ministry of Culture, Sports and Tourism (RS-2024-00332210), and under the artificial intelligence semiconductor support program to nurture the best talents (IITP-(2025)-RS-2023-00253914) and by the Artificial Intelligence Graduate School Program (RS-2020-II201373, Hanyang University) grant funded by the Korea government, and by the MSIT (RS-2023-00261368). Data collection and sharing for the Alzheimer's Disease Neuroimaging Initiative (ADNI) is funded by the National Institute on Aging (National Institutes of Health Grant U19 AG024904). The grantee organization is the Northern California Institute for Research and Education. In the past, ADNI has also received funding from the National Institute of Biomedical Imaging and Bioengineering, the Canadian Institutes of Health Research, and private sector contributions through the Foundation for the National Institutes of Health (FNIH) including generous contributions from the following: AbbVie, Alzheimer's Association; Alzheimer's Drug Discovery Foundation; Araclon Biotech; BioClinica, Inc.; Biogen; Bristol-Myers Squibb Company; CereSpir, Inc.; Cogstate; Eisai Inc.; Elan Pharmaceuticals, Inc.; Eli Lilly and Company; EuroImmun; F. Hoffmann-La Roche Ltd and its affiliated company Genentech, Inc.; Fujirebio; GE Healthcare; IXICO Ltd.; Janssen Alzheimer Immunotherapy Research & Development, LLC.; Johnson & Johnson Pharmaceutical Research & Development LLC.; Lumosity; Lundbeck; Merck & Co., Inc.; Meso Scale Diagnostics, LLC.; NeuroRx Research; Neurotrack Technologies; Novartis Pharmaceuticals Corporation; Pfizer Inc.; Piramal Imaging; Servier; Takeda Pharmaceutical Company; and Transition Therapeutics.

References

- Abu-Srhan, A., Almallahi, I., Abushariah, M.A., Mahafza, W., Al-Kadi, O.S., 2021. Paired-unpaired unsupervised attention guided gan with transfer learning for bidirectional brain mr-ct synthesis. *Computers in Biology and Medicine* 136, 104763. doi:10.1016/j.combiomed.2021.104763.
- Armanious, K., Jiang, C., Abdulatif, S., Küstner, T., Gatidis, S., Yang, B., 2019. Unsupervised medical image translation using cycle-medgan, in: 2019 27th European signal processing conference (EUSIPCO), IEEE. pp. 1–5. doi:10.23919/EUSIPCO.2019.8902799.

- Armanious, K., Jiang, C., Fischer, M., Küstner, T., Hepp, T., Nikolaou, K., Gatidis, S., Yang, B., 2020. Medgan: Medical image translation using gans. *Computerized medical imaging and graphics* 79, 101684. doi:10.1016/j.compmedimag.2019.101684.
- Barthélemy, N.R., Salvadó, G., Schindler, S.E., He, Y., Janelidze, S., Collij, L.E., Saef, B., Henson, R.L., Chen, C.D., Gordon, B.A., et al., 2024. Highly accurate blood test for alzheimer’s disease is similar or superior to clinical cerebrospinal fluid tests. *Nature medicine* 30, 1085–1095. doi:10.1038/s41591-024-02869-z.
- Berger, M., Gould, M.K., Barnett, P.G., 2003. The cost of positron emission tomography in six united states veterans affairs hospitals and two academic medical centers. *American journal of roentgenology* 181, 359–365.
- Braak, H., Alafuzoff, I., Arzberger, T., Kretschmar, H., Del Tredici, K., 2006. Staging of alzheimer disease-associated neurofibrillary pathology using paraffin sections and immunocytochemistry. *Acta neuropathologica* 112, 389–404.
- Braak, H., Braak, E., 1991. Neuropathological staging of alzheimer-related changes. *Acta neuropathologica* 82, 239–259.
- Buchhave, P., Minthon, L., Zetterberg, H., Wallin, Å.K., Blennow, K., Hansson, O., 2012. Cerebrospinal fluid levels of β -amyloid 1-42, but not of tau, are fully changed already 5 to 10 years before the onset of alzheimer dementia. *Archives of general psychiatry* 69, 98–106. doi:10.1001/archgenpsychiatry.2011.155.
- Buck, A.K., Herrmann, K., Stargardt, T., Dechow, T., Krause, B.J., Schreyögg, J., 2010. Economic evaluation of pet and pet/ct in oncology: evidence and methodologic approaches. *Journal of nuclear medicine technology* 38, 6–17.
- Cardoso, M.J., Li, W., Brown, R., Ma, N., Kerfoot, E., Wang, Y., Murray, B., Myronenko, A., Zhao, C., Yang, D., Nath, V., He, Y., Xu, Z., Hatamizadeh, A., Zhu, W., Liu, Y., Zheng, M., Tang, Y., Yang, I., Zephyr, M., Hashemian, B., Alle, S., Zalbagi Darestani, M., Budd, C., Modat, M., Vercauteren, T., Wang, G., Li, Y., Hu, Y., Fu, Y., Gorman, B., Johnson, H., Genereaux, B., Erdal, B.S., Gupta, V., Diaz-Pinto, A., Dourson, A., Maier-Hein, L., Jaeger, P.F., Baumgartner, M., Kalpathy-Cramer, J., Flores, M., Kirby, J., Cooper, L.A., Roth, H.R., Xu, D., Bericat, D., Floca, R., Zhou, S.K., Shuaib, H., Farahani, K., Maier-Hein, K.H., Aylward, S., Dogra, P., Ourselin, S., Feng, A., 2022. MONAI: An open-source framework for deep learning in healthcare doi:10.48550/arXiv.2211.02701.
- Chen, S., Ma, K., Zheng, Y., 2019. Med3d: Transfer learning for 3d medical image analysis. arXiv preprint arXiv:1904.00625 doi:10.48550/arXiv.1904.00625.
- Chen, S.D., Lu, J.Y., Li, H.Q., Yang, Y.X., Jiang, J.H., Cui, M., Zuo, C.T., Tan, L., Dong, Q., Yu, J.T., et al., 2021. Staging tau pathology with tau pet in alzheimer’s disease: a longitudinal study. *Translational psychiatry* 11, 483.
- Cho, H., Choi, J.Y., Hwang, M.S., Lee, J.H., Kim, Y.J., Lee, H.M., Lyoo, C.H., Ryu, Y.H., Lee, M.S., 2016. Tau pet in alzheimer disease and mild cognitive impairment. *Neurology* 87, 375–383. doi:10.1212/WNL.0000000000002892.

- Çiçek, Ö., Abdulkadir, A., Lienkamp, S.S., Brox, T., Ronneberger, O., 2016. 3d u-net: learning dense volumetric segmentation from sparse annotation, in: Medical Image Computing and Computer-Assisted Intervention–MICCAI 2016: 19th International Conference, Athens, Greece, October 17-21, 2016, Proceedings, Part II 19, Springer. pp. 424–432. doi:10.1007/978-3-319-46723-8_49.
- Cummings, J., Osse, A.M.L., Cammann, D., Powell, J., Chen, J., 2024. Anti-amyloid monoclonal antibodies for the treatment of alzheimer’s disease. *BioDrugs* 38, 5–22.
- Dale, A.M., Fischl, B., Sereno, M.I., 1999. Cortical surface-based analysis: I. segmentation and surface reconstruction. *Neuroimage* 9, 179–194. doi:10.1006/nimg.1998.0395.
- Dar, S.U., Yurt, M., Karacan, L., Erdem, A., Erdem, E., Cukur, T., 2019. Image synthesis in multi-contrast mri with conditional generative adversarial networks. *IEEE transactions on medical imaging* 38, 2375–2388. doi:10.1109/TMI.2019.2901750.
- Dayarathna, S., Islam, K.T., Uribe, S., Yang, G., Hayat, M., Chen, Z., 2023. Deep learning based synthesis of mri, ct and pet: Review and analysis. *Medical Image Analysis* , 103046doi:10.1016/j.media.2023.103046.
- Dietlein, M., Weber, K., Gandjour, A., Moka, D., Theissen, P., Lauterbach, K.W., Schicha, H., 2000. Cost-effectiveness of fdg-pet for the management of potentially operable non-small cell lung cancer: priority for a pet-based strategy after nodal-negative ct results. *European journal of nuclear medicine* 27, 1598–1609.
- Du, J., Li, W., Lu, K., Xiao, B., 2016. An overview of multi-modal medical image fusion. *Neurocomputing* 215, 3–20.
- Gambhir, S.S., 2002. Molecular imaging of cancer with positron emission tomography. *Nature Reviews Cancer* 2, 683–693.
- Goodfellow, I., Pouget-Abadie, J., Mirza, M., Xu, B., Warde-Farley, D., Ozair, S., Courville, A., Bengio, Y., 2014. Generative adversarial nets. *Advances in neural information processing systems* 27. URL: https://proceedings.neurips.cc/paper_files/paper/2014/file/5ca3e9b122f61f8f06494c97b1afccf3-Paper.pdf.
- Guo, Y., Huang, Y.Y., Shen, X.N., Chen, S.D., Hu, H., Wang, Z.T., Tan, L., Yu, J.T., Initiative, A.D.N., 2021. Characterization of alzheimer’s tau biomarker discordance using plasma, csf, and pet. *Alzheimer’s research & therapy* 13, 93. doi:10.1186/s13195-021-00834-3.
- Ha, J., Wang, N., Maharjan, S., Zhang, X., 2024. 3d volumetric super-resolution in radiology using 3d rrdg-gan. *arXiv preprint arXiv:2402.04171* doi:10.48550/arXiv.2402.04171.
- Hatamizadeh, A., Nath, V., Tang, Y., Yang, D., Roth, H.R., Xu, D., 2021. Swin unetr: Swin transformers for semantic segmentation of brain tumors in mri images, in: International MICCAI Brainlesion Workshop, Springer. pp. 272–284. doi:10.1007/978-3-031-08999-2_22.

- Hatamizadeh, A., Tang, Y., Nath, V., Yang, D., Myronenko, A., Landman, B., Roth, H.R., Xu, D., 2022. Unetr: Transformers for 3d medical image segmentation, in: Proceedings of the IEEE/CVF winter conference on applications of computer vision, pp. 574–584. doi:10.1109/WACV51458.2022.00181.
- He, K., Zhang, X., Ren, S., Sun, J., 2016. Deep residual learning for image recognition, in: Proceedings of the IEEE conference on computer vision and pattern recognition, pp. 770–778.
- Ho, J., Jain, A., Abbeel, P., 2020. Denoising diffusion probabilistic models, in: Advances in Neural Information Processing Systems, Curran Associates, Inc.. pp. 6840–6851. URL: https://proceedings.neurips.cc/paper_files/paper/2020/file/4c5bcfec8584af0d967f1ab10179ca4b-Paper.pdf.
- Hoopes, A., Mora, J.S., Dalca, A.V., Fischl, B., Hoffmann, M., 2022. Synthstrip: skull-stripping for any brain image. *NeuroImage* 260, 119474. doi:10.1016/j.neuroimage.2022.119474.
- Hu, S., Lei, B., Wang, S., Wang, Y., Feng, Z., Shen, Y., 2021. Bidirectional mapping generative adversarial networks for brain mr to pet synthesis. *IEEE Transactions on Medical Imaging* 41, 145–157. doi:10.1109/TMI.2021.3107013.
- Igarashi, K.M., 2023. Entorhinal cortex dysfunction in alzheimer’s disease. *Trends in neurosciences* 46, 124–136.
- Insel, P.S., Mormino, E.C., Aisen, P.S., Thompson, W.K., Donohue, M.C., 2020. Neuroanatomical spread of amyloid β and tau in alzheimer’s disease: implications for primary prevention. *Brain Communications* 2, fcaa007.
- Ioffe, S., Szegedy, C., 2015. Batch normalization: Accelerating deep network training by reducing internal covariate shift, in: International conference on machine learning, pmlr. pp. 448–456.
- Isola, P., Zhu, J.Y., Zhou, T., Efros, A.A., 2017. Image-to-image translation with conditional adversarial networks, in: Proceedings of the IEEE conference on computer vision and pattern recognition, pp. 1125–1134. doi:10.1109/CVPR.2017.632.
- Jack, C.R., Knopman, D.S., Jagust, W.J., Shaw, L.M., Aisen, P.S., Weiner, M.W., Petersen, R.C., Trojanowski, J.Q., 2010. Hypothetical model of dynamic biomarkers of the alzheimer’s pathological cascade. *The Lancet Neurology* 9, 119–128.
- Jack Jr, C.R., Bennett, D.A., Blennow, K., Carrillo, M.C., Dunn, B., Haeberlein, S.B., Holtzman, D.M., Jagust, W., Jessen, F., Karlawish, J., et al., 2018. Nia-aa research framework: toward a biological definition of alzheimer’s disease. *Alzheimer’s & dementia* 14, 535–562.
- Jack Jr, C.R., Wiste, H.J., Weigand, S.D., Therneau, T.M., Lowe, V.J., Knopman, D.S., Botha, H., Graff-Radford, J., Jones, D.T., Ferman, T.J., et al., 2020. Predicting future rates of tau accumulation on pet. *Brain* 143, 3136–3150.

- Jang, S.I., Lois, C., Thibault, E., Becker, J.A., Dong, Y., Normandin, M.D., Price, J.C., Johnson, K.A., Fakhri, G.E., Gong, K., 2023. Taupetgen: Text-conditional tau pet image synthesis based on latent diffusion models. arXiv preprint arXiv:2306.11984 doi:10.48550/arXiv.2306.11984.
- Johnson, J., Alahi, A., Fei-Fei, L., 2016. Perceptual losses for real-time style transfer and super-resolution, in: *Computer Vision—ECCV 2016: 14th European Conference, Amsterdam, The Netherlands, October 11–14, 2016, Proceedings, Part II 14*, Springer. pp. 694–711. doi:10.1007/978-3-319-46475-6_43.
- Kingma, D.P., Ba, J., 2015. Adam: A method for stochastic optimization, in: *3rd International Conference on Learning Representations*.
- Knopman, D.S., Amieva, H., Petersen, R.C., Chételat, G., Holtzman, D.M., Hyman, B.T., Nixon, R.A., Jones, D.T., 2021. Alzheimer disease. *Nature reviews Disease primers* 7, 33. doi:10.1038/s41572-021-00269-y.
- Lee, J., Burkett, B.J., Min, H.K., Senjem, M.L., Dicks, E., Corriveau-Lecavalier, N., Mester, C.T., Wiste, H.J., Lundt, E.S., Murray, M.E., et al., 2024. Synthesizing images of tau pathology from cross-modal neuroimaging using deep learning. *Brain* 147, 980–995.
- Leuzy, A., Chiotis, K., Lemoine, L., Gillberg, P.G., Almkvist, O., Rodriguez-Vieitez, E., Nordberg, A., 2019. Tau pet imaging in neurodegenerative tauopathies—still a challenge. *Molecular psychiatry* 24, 1112–1134. doi:10.1038/s41380-018-0342-8.
- Li, Y., Yakushev, I., Hedderich, D.M., Wachinger, C., 2024. Pasta: Pathology-aware mri to pet cross-modal translation with diffusion models, in: *International Conference on Medical Image Computing and Computer-Assisted Intervention*, Springer. pp. 529–540.
- Liu, Y., Chen, H., Chen, Y., Yin, W., Shen, C., 2021. Generic perceptual loss for modeling structured output dependencies, in: *Proceedings of the IEEE/CVF Conference on Computer Vision and Pattern Recognition*, pp. 5424–5432. doi:10.1109/CVPR46437.2021.00538.
- Loshchilov, I., Hutter, F., 2017. SGDR: Stochastic gradient descent with warm restarts, in: *5th International Conference on Learning Representations*. URL: <https://openreview.net/forum?id=Skq89Scxx>.
- Lowe, V.J., Wiste, H.J., Senjem, M.L., Weigand, S.D., Therneau, T.M., Boeve, B.F., Josephs, K.A., Fang, P., Pandey, M.K., Murray, M.E., et al., 2018. Widespread brain tau and its association with ageing, braak stage and alzheimer’s dementia. *Brain* 141, 271–287.
- Maass, A., Landau, S., Baker, S.L., Horng, A., Lockhart, S.N., La Joie, R., Rabinovici, G.D., Jagust, W.J., Initiative, A.D.N., et al., 2017. Comparison of multiple tau-pet measures as biomarkers in aging and alzheimer’s disease. *Neuroimage* 157, 448–463.

- Mattay, V.S., Fotenos, A.F., Ganley, C.J., Marzella, L., 2020. Brain tau imaging: Food and drug administration approval of 18f-flortaucipir injection. *Journal of Nuclear Medicine* 61, 1411–1412. URL: <https://jnm.snmjournals.org/content/61/10/1411>, doi:10.2967/jnumed.120.252254.
- Mei, X., Liu, Z., Robson, P.M., Marinelli, B., Huang, M., Doshi, A., Jacobi, A., Cao, C., Link, K.E., Yang, T., et al., 2022. Radimagenet: an open radiologic deep learning research dataset for effective transfer learning. *Radiology: Artificial Intelligence* 4, e210315.
- Mitchell, T.W., Mufson, E.J., Schneider, J.A., Cochran, E.J., Nissanov, J., Han, L.Y., Bienias, J.L., Lee, V.M.Y., Trojanowski, J.Q., Bennett, D.A., et al., 2002. Parahippocampal tau pathology in healthy aging, mild cognitive impairment, and early alzheimer’s disease. *Annals of Neurology: Official Journal of the American Neurological Association and the Child Neurology Society* 51, 182–189.
- Nie, D., Trullo, R., Lian, J., Wang, L., Petitjean, C., Ruan, S., Wang, Q., Shen, D., 2018. Medical image synthesis with deep convolutional adversarial networks. *IEEE Transactions on Biomedical Engineering* 65, 2720–2730. doi:10.1109/TBME.2018.2814538.
- Ortner, M., Drost, R., Hedderich, D., Goldhardt, O., Müller-Sarnowski, F., Diehl-Schmid, J., Förstl, H., Yakushev, I., Grimmer, T., 2019. Amyloid pet, fdg-pet or mri?-the power of different imaging biomarkers to detect progression of early alzheimer’s disease. *BMC neurology* 19, 1–6.
- Pan, S., Chang, C.W., Peng, J., Zhang, J., Qiu, R.L., Wang, T., Roper, J., Liu, T., Mao, H., Yang, X., 2023. Cycle-guided denoising diffusion probability model for 3d cross-modality mri synthesis. arXiv preprint arXiv:2305.00042 doi:10.48550/arXiv.2305.00042.
- Pan, Y., Liu, M., Lian, C., Xia, Y., Shen, D., 2020. Spatially-constrained fisher representation for brain disease identification with incomplete multi-modal neuroimages. *IEEE transactions on medical imaging* 39, 2965–2975.
- Pascoal, T.A., Benedet, A.L., Ashton, N.J., Kang, M.S., Therriault, J., Chamoun, M., Savard, M., Lussier, F.Z., Tissot, C., Karikari, T.K., et al., 2021. Microglial activation and tau propagate jointly across braak stages. *Nature medicine* 27, 1592–1599.
- Petersen, G.C., Roytman, M., Chiang, G.C., Li, Y., Gordon, M.L., Franceschi, A.M., 2022. Overview of tau pet molecular imaging. *Current opinion in neurology* 35, 230–239. doi:10.1097/WCO.0000000000001035.
- Pleen, J., Camerucci, E., Al-Sabbagh, M.Q., Cunningham, K., 2024. Blood-based biomarkers in alzheimer disease. *PRACTICAL NEUROLOGY* .
- Pooler, A.M., Polydoro, M., Wegmann, S., Nicholls, S.B., Spires-Jones, T.L., Hyman, B.T., 2013. Propagation of tau pathology in alzheimer’s disease: identification of novel therapeutic targets. *Alzheimer’s research & therapy* 5, 1–8. doi:10.1186/alzrt214.
- Rasmussen, J., Langerman, H., 2019. Alzheimer’s disease-why we need early diagnosis. *Degenerative neurological and neuromuscular disease* , 123–130doi:10.2147/DNND.S228939.

- Ronneberger, O., Fischer, P., Brox, T., 2015. U-net: Convolutional networks for biomedical image segmentation, in: Medical image computing and computer-assisted intervention–MICCAI 2015: 18th international conference, Munich, Germany, October 5-9, 2015, proceedings, part III 18, Springer. pp. 234–241. doi:10.1007/978-3-319-24574-4_28.
- Russakovsky, O., Deng, J., Su, H., Krause, J., Satheesh, S., Ma, S., Huang, Z., Karpathy, A., Khosla, A., Bernstein, M., et al., 2015. Imagenet large scale visual recognition challenge. *International journal of computer vision* 115, 211–252.
- Saif, M.W., Tzannou, I., Makrilia, N., Syrigos, K., 2010. Role and cost effectiveness of pet/ct in management of patients with cancer. *The Yale journal of biology and medicine* 83, 53.
- Seemiller, J., Bischof, G.N., Hoenig, M.C., Tahmasian, M., van Eimeren, T., Drzezga, A., Initiative, A.D.N., 2021. Indication of retrograde tau spreading along braak stages and functional connectivity pathways. *European journal of nuclear medicine and molecular imaging* 48, 2272–2282.
- Shaw, L.M., Arias, J., Blennow, K., Galasko, D., Molinuevo, J.L., Salloway, S., Schindler, S., Carrillo, M.C., Hendrix, J.A., Ross, A., et al., 2018. Appropriate use criteria for lumbar puncture and cerebrospinal fluid testing in the diagnosis of alzheimer’s disease. *Alzheimer’s & Dementia* 14, 1505–1521.
- Shin, H.C., Ihsani, A., Xu, Z., Mandava, S., Sreenivas, S.T., Forster, C., Cha, J., Initiative, A.D.N., 2020. Gandalf: Generative adversarial networks with discriminator-adaptive loss fine-tuning for alzheimer’s disease diagnosis from mri, in: Medical Image Computing and Computer Assisted Intervention–MICCAI 2020: 23rd International Conference, Lima, Peru, October 4–8, 2020, Proceedings, Part II 23, Springer. pp. 688–697. doi:10.1007/978-3-030-59713-9_66.
- Sikka, A., Peri, S.V., Bathula, D.R., 2018. Mri to fdg-pet: cross-modal synthesis using 3d u-net for multi-modal alzheimer’s classification, in: Simulation and Synthesis in Medical Imaging: Third International Workshop, SASHIMI 2018, Held in Conjunction with MICCAI 2018, Granada, Spain, September 16, 2018, Proceedings 3, Springer. pp. 80–89. doi:10.1007/978-3-030-00536-8_9.
- Sled, J.G., Zijdenbos, A.P., Evans, A.C., 1998. A nonparametric method for automatic correction of intensity nonuniformity in mri data. *IEEE transactions on medical imaging* 17, 87–97. doi:10.1109/42.668698.
- Slough, C., Masters, S.C., Hurley, R.A., Taber, K.H., 2016. Clinical positron emission tomography (pet) neuroimaging: advantages and limitations as a diagnostic tool. *The Journal of neuropsychiatry and clinical neurosciences* 28, A4–71.
- Smith, L.N., 2017. Cyclical learning rates for training neural networks, in: 2017 IEEE winter conference on applications of computer vision (WACV), IEEE. pp. 464–472. doi:10.1109/WACV.2017.58.

- Srivastava, N., Hinton, G., Krizhevsky, A., Sutskever, I., Salakhutdinov, R., 2014. Dropout: a simple way to prevent neural networks from overfitting. *The journal of machine learning research* 15, 1929–1958.
- Szegedy, C., Vanhoucke, V., Ioffe, S., Shlens, J., Wojna, Z., 2016. Rethinking the inception architecture for computer vision, in: *Proceedings of the IEEE conference on computer vision and pattern recognition*, pp. 2818–2826.
- The General Hospital Corporation (MGH), 2023. Freesurfer. URL: <https://surfer.nmr.mgh.harvard.edu>. version 7.4.1.
- Ulyanov, D., Vedaldi, A., Lempitsky, V., 2016. Instance normalization: The missing ingredient for fast stylization. *arXiv preprint arXiv:1607.08022* doi:10.48550/arXiv.1607.08022.
- Van Dyck, C.H., Swanson, C.J., Aisen, P., Bateman, R.J., Chen, C., Gee, M., Kanekiyo, M., Li, D., Reyderman, L., Cohen, S., et al., 2023. Lecanemab in early alzheimer’s disease. *New England Journal of Medicine* 388, 9–21.
- Van Hoesen, G.W., Hyman, B.T., Damasio, A.R., 1991. Entorhinal cortex pathology in alzheimer’s disease. *Hippocampus* 1, 1–8.
- Vaquero, J.J., Kinahan, P., 2015. Positron emission tomography: current challenges and opportunities for technological advances in clinical and preclinical imaging systems. *Annual review of biomedical engineering* 17, 385–414. doi:10.1146/annurev-bioeng-071114-040723.
- Vaswani, A., Shazeer, N., Parmar, N., Uszkoreit, J., Jones, L., Gomez, A.N., Kaiser, Ł., Polosukhin, I., 2017. Attention is all you need. *Advances in neural information processing systems* 30.
- Wang, C., Piao, S., Huang, Z., Gao, Q., Zhang, J., Li, Y., Shan, H., Initiative, A.D.N., et al., 2024. Joint learning framework of cross-modal synthesis and diagnosis for alzheimer’s disease by mining underlying shared modality information. *Medical Image Analysis* 91, 103032.
- Wang, R., Chopra, N., Nho, K., Maloney, B., Obukhov, A.G., Nelson, P.T., Counts, S.E., Lahiri, D.K., 2022. Human microrna (mir-20b-5p) modulates alzheimer’s disease pathways and neuronal function, and a specific polymorphism close to the mir20b gene influences alzheimer’s biomarkers. *Molecular psychiatry* 27, 1256–1273.
- Wang, Z., Bovik, A.C., Sheikh, H.R., Simoncelli, E.P., 2004. Image quality assessment: from error visibility to structural similarity. *IEEE transactions on image processing* 13, 600–612. doi:10.1109/TIP.2003.819861.
- Winblad, B., Amouyel, P., Andrieu, S., Ballard, C., Brayne, C., Brodaty, H., Cedazo-Minguez, A., Dubois, B., Edvardsson, D., Feldman, H., et al., 2016. Defeating alzheimer’s disease and other dementias: a priority for european science and society. *The Lancet Neurology* 15, 455–532.

- Wong, W., 2020. Economic burden of alzheimer disease and managed care considerations. *The American journal of managed care* 26, S177–S183.
- Xie, T., Cao, C., Cui, Z., Guo, Y., Wu, C., Wang, X., Li, Q., Hu, Z., Sun, T., Sang, Z., et al., 2023. Synthesizing pet images from high-field and ultra-high-field mr images using joint diffusion attention model. *arXiv preprint arXiv:2305.03901* doi:10.48550/arXiv.2305.03901.
- Yang, H., Sun, J., Carass, A., Zhao, C., Lee, J., Xu, Z., Prince, J., 2018. Unpaired brain mr-to-ct synthesis using a structure-constrained cyclegan, in: *Deep Learning in Medical Image Analysis and Multimodal Learning for Clinical Decision Support: 4th International Workshop, DLMIA 2018, and 8th International Workshop, ML-CDS 2018, Held in Conjunction with MICCAI 2018, Granada, Spain, September 20, 2018, Proceedings 4*, Springer. pp. 174–182. doi:10.1007/978-3-030-00889-5_20.
- Yu, B., Wang, Y., Wang, L., Shen, D., Zhou, L., 2020. Medical image synthesis via deep learning. *Deep Learning in Medical Image Analysis: Challenges and Applications* , 23–44doi:10.1007/978-3-030-33128-3_2.
- Zhang, J., He, X., Qing, L., Gao, F., Wang, B., 2022. Bpgan: Brain pet synthesis from mri using generative adversarial network for multi-modal alzheimer’s disease diagnosis. *Computer Methods and Programs in Biomedicine* 217, 106676. doi:10.1016/j.cmpb.2022.106676.
- Zhao, P., Pan, H., Xia, S., 2021. Mri-trans-gan: 3d mri cross-modality translation, in: *2021 40th Chinese Control Conference (CCC)*, IEEE. pp. 7229–7234. doi:10.23919/CCC52363.2021.9550256.
- Zhu, J.Y., Park, T., Isola, P., Efros, A.A., 2017. Unpaired image-to-image translation using cycle-consistent adversarial networks, in: *Proceedings of the IEEE international conference on computer vision*, pp. 2223–2232. doi:10.1109/ICCV.2017.244.
- Zhu, Y., Zhu, X., 2019. Mri-driven pet image optimization for neurological applications. *Frontiers in Neuroscience* 13, 782.

Cyclic 2.5D Perceptual Loss for Cross-Modal 3D Medical Image Synthesis: T1w MRI to Tau PET —Supplementary Materials—

Junho Moon^a, Symac Kim^b, Haejun Chung^{a,b,c,†}, Ikbeom Jang^{d,e,f,†}, for the Alzheimer’s
Disease Neuroimaging Initiative*

^aDepartment of Artificial Intelligence Semiconductor Engineering, Hanyang University, Seoul, South Korea

^bDepartment of Artificial Intelligence, Hanyang University, Seoul, South Korea

^cDepartment of Electronic Engineering, Hanyang University, Seoul, South Korea

^dDivision of Computer Engineering, Hankuk University of Foreign Studies, Yongin, South Korea

^eDivision of AI Data Convergence, Hankuk University of Foreign Studies, Yongin, South Korea

^fDivision of Language & AI, Hankuk University of Foreign Studies, Yongin, South Korea

Contents

| | |
|---|----------|
| A Additional Experimental Results | 1 |
| A.1 Cyclic 2.5D Perceptual Loss Model Selection | 1 |
| A.2 Comprehensive Benchmark Results | 1 |
| A.3 ROI Analysis Across All Cortical Regions | 2 |
| A.4 Ablation Study on Preprocessing Steps | 4 |

A. Additional Experimental Results

A.1. Cyclic 2.5D Perceptual Loss Model Selection

Table 1 presents the overall experimental results for selecting the perceptual loss model ϕ and the weight λ for perceptual loss. The cyclic 2.5D perceptual loss was tested with λ values of $\{0.1, 0.5, 1, 3, 5\}$ across all the perceptual loss models used in these experiments. The highest performance was achieved when utilizing features extracted from the 23rd layer (10th ReLU) of the VGG-16 model (Simonyan and Zisserman, 2015) for perceptual loss calculation. Based on these findings, the perceptual loss model ϕ was fixed as VGG-16, the feature extraction layer j as 23 (10th ReLU), and the weight λ as 0.5 for all subsequent experiments.

[†]Corresponding authors

Email addresses: haejun@hanyang.ac.kr (Haejun Chung), ijang@hufs.ac.kr (Ikbeom Jang)

*Data used in preparation of this article were obtained from the Alzheimer’s Disease Neuroimaging Initiative (ADNI) database (adni.loni.usc.edu). As such, the investigators within the ADNI contributed to the design and implementation of ADNI and/or provided data but did not participate in analysis or writing of this report. A complete listing of ADNI investigators can be found at: http://adni.loni.usc.edu/wp-content/uploads/how_to_apply/ADNI_Acknowledgement_List.pdf

| Dataset | Perceptual Loss Model (ϕ) | Feature Extraction Layer (j) | n_{params} | Perceptual Loss Weight (λ) | SSIM(%) \uparrow | PSNR(dB) \uparrow | MAE \downarrow |
|-------------|----------------------------------|----------------------------------|---------------------|--------------------------------------|----------------------------------|---------------------------------|------------------|
| RadImageNet | ResNet-50 | 3rd Block Stack | 8.53M | 0.1 | 90.30 \pm 3.74 | 28.94 \pm 3.17 | 10.30 \pm 4.66 |
| | | | | 0.5 | 90.37 \pm 3.63 | 28.99 \pm 3.06 | 10.09 \pm 4.62 |
| | | | | 1.0 | 90.37 \pm 3.58 | 29.03 \pm 3.09 | 10.05 \pm 4.85 |
| | | | | 3.0 | 89.97 \pm 3.54 | 28.94 \pm 2.96 | 10.02 \pm 4.59 |
| | | | | 5.0 | 89.71 \pm 3.57 | 28.68 \pm 2.89 | 10.37 \pm 4.94 |
| | InceptionNet v3 | 8th Inception Module | 8.97M | 0.1 | 90.45 \pm 3.68 | 29.06 \pm 3.17 | 10.11 \pm 4.80 |
| | | | | 0.5 | 90.48 \pm 3.67 | 29.11 \pm 3.18 | 10.03 \pm 4.79 |
| | | | | 1.0 | 90.45 \pm 3.64 | 29.08 \pm 3.10 | 10.05 \pm 4.79 |
| | | | | 3.0 | 90.08 \pm 3.62 | 28.87 \pm 2.97 | 10.34 \pm 4.71 |
| | | | | 5.0 | 89.99 \pm 3.67 | 28.90 \pm 2.99 | 10.24 \pm 4.72 |
| ImageNet-1K | ResNet-50 | 3rd Block Stack | 8.53M | 0.1 | 90.48 \pm 3.65 | 29.03 \pm 3.12 | 10.05 \pm 4.87 |
| | | | | 0.5 | 90.45 \pm 3.68 | 29.06 \pm 3.16 | 9.99 \pm 4.97 |
| | | | | 1.0 | 90.31 \pm 3.72 | 29.01 \pm 3.12 | 10.00 \pm 4.98 |
| | | | | 3.0 | 89.94 \pm 3.70 | 28.86 \pm 3.03 | 10.17 \pm 4.83 |
| | | | | 5.0 | 89.41 \pm 3.84 | 28.64 \pm 3.15 | 10.49 \pm 5.19 |
| | InceptionNet v3 | 8th Inception Module | 8.97M | 0.1 | 90.20 \pm 3.77 | 28.72 \pm 3.11 | 10.46 \pm 4.60 |
| | | | | 0.5 | 90.65 \pm 3.57 | 29.30 \pm 3.09 | 9.79 \pm 4.65 |
| | | | | 1.0 | 90.51 \pm 3.59 | 29.20 \pm 3.04 | 9.85 \pm 4.76 |
| | | | | 3.0 | 90.34 \pm 3.56 | 28.99 \pm 2.90 | 10.04 \pm 4.63 |
| | | | | 5.0 | 90.43 \pm 3.67 | 29.16 \pm 3.04 | 9.86 \pm 4.64 |
| VGG-16 | 10th ReLU | 7.63M | 0.1 | 90.41 \pm 3.71 | 28.95 \pm 3.20 | 10.22 \pm 4.56 | |
| | | | 0.5 | 90.69\pm3.59 | 29.31\pm3.19 | 9.73\pm4.83 | |
| | | | 1.0 | 90.43 \pm 3.67 | 29.18 \pm 3.19 | 9.86 \pm 4.90 | |
| | | | 3.0 | 89.92 \pm 3.71 | 28.82 \pm 3.16 | 10.22 \pm 4.97 | |
| | | | 5.0 | 89.86 \pm 3.64 | 28.81 \pm 2.95 | 10.17 \pm 4.72 | |

Table 1: Overall experimental results for selecting cyclic 2.5D perceptual loss model ϕ and optimal weight λ . The evaluations were conducted using the validation set. The perceptual loss weight λ was systematically tested with values of $\{0.1, 0.5, 1, 3, 5\}$ for each model. The feature extraction layers were selected while maintaining comparable parameter counts across the model. In all experiments, image translation was performed using a 3D U-Net (Çiçek et al., 2016) model. The results are reported as mean \pm standard deviation. Note: The SSIM, PSNR, or MAE values represent performance across the 3D volume.

A.2. Comprehensive Benchmark Results

Table 2 provides the comprehensive experimental results comparing the cyclic 2.5D perceptual loss with benchmark methods. The table reports quantitative metrics, including structural similarity index measure (SSIM), peak signal-to-noise ratio (PSNR), and normalized mean absolute error (NMAE), across overall (3D) performance and individual 2D views in the axial, coronal, and sagittal planes. Rows marked with a dagger symbol (\dagger) correspond to experiments conducted on PET data preprocessed via by-manufacturer standardization. In contrast, rows without the dagger indicate results from PET data preprocessed with min-max normalization. Under by-manufacturer standardization, PET SUVR values are not scaled to a fixed range (e.g., -1 to 1), distinguishing it from min-max normalization. Thus, the mean absolute error (MAE) was replaced with the NMAE to ensure a fair comparison across preprocessing methods. The NMAE is computed by normalizing the MAE with respect to the range of the ground truth PET SUVR values (y), as defined below:

$$NMAE(\hat{y}, y) = \frac{MAE}{\max(y) - \min(y)} \quad (1)$$

| Model | Perceptual Loss | SSIM(%) \uparrow | | | PSNR(dB) \uparrow | | | NMAE \downarrow | | | | | |
|---------------------------|--------------------|----------------------------------|----------------------------------|----------------------------------|----------------------------------|----------------------------------|----------------------------------|----------------------------------|----------------------------------|---------------------------------|---------------------------------|---------------------------------|---------------------------------|
| | | Overall (3D) | Axial | Coronal | Sagittal | Overall (3D) | Axial | Coronal | Sagittal | Overall (3D) | Axial | Coronal | Sagittal |
| PASTA w/ MRI only | None | 85.32 \pm 4.49 | 80.79 \pm 5.28 | 80.26 \pm 4.81 | 79.10 \pm 5.12 | 24.98 \pm 2.88 | 25.98 \pm 3.52 | 23.55 \pm 2.87 | 24.22 \pm 3.07 | 2.35 \pm 0.98 | 3.30 \pm 1.27 | 3.41 \pm 1.31 | 3.60 \pm 1.44 |
| ShareGAN w/ AD vs. MCI | None | 85.40 \pm 4.59 | 79.98 \pm 6.06 | 79.41 \pm 5.85 | 78.02 \pm 6.53 | 25.01 \pm 2.57 | 26.19 \pm 4.32 | 23.57 \pm 2.48 | 24.24 \pm 2.86 | 2.17 \pm 0.87 | 3.15 \pm 1.32 | 3.23 \pm 1.23 | 3.43 \pm 1.34 |
| U-Net | 3D | 87.18 \pm 5.47 | 82.23 \pm 6.71 | 82.12 \pm 7.03 | 80.89 \pm 7.62 | 25.51 \pm 1.99 | 25.01 \pm 1.80 | 24.48 \pm 2.12 | 24.44 \pm 2.16 | 3.91 \pm 0.72 | 4.47 \pm 0.91 | 4.50 \pm 1.00 | 4.64 \pm 1.07 |
| | 2.5D | 85.33 \pm 5.35 | 80.40 \pm 6.48 | 80.18 \pm 6.80 | 79.03 \pm 7.37 | 23.09 \pm 1.47 | 22.74 \pm 1.44 | 22.55 \pm 1.66 | 22.52 \pm 1.70 | 6.06 \pm 1.00 | 6.40 \pm 1.09 | 6.38 \pm 1.16 | 6.45 \pm 1.20 |
| U-Net [†] | Cyclic 2.5D (Ours) | 88.09\pm5.89 | 82.78\pm7.59 | 82.79\pm7.59 | 81.49\pm8.26 | 26.71\pm2.81 | 26.56\pm2.68 | 25.32\pm2.83 | 25.48\pm2.87 | 2.56\pm0.86 | 3.29\pm1.16 | 3.35\pm1.21 | 3.51\pm1.30 |
| | 2.5D | 89.81 \pm 3.69 | 85.83 \pm 4.44 | 85.82 \pm 4.40 | 84.60 \pm 4.70 | 28.34 \pm 2.65 | 29.17 \pm 3.71 | 27.09 \pm 2.53 | 27.49 \pm 2.79 | 1.49 \pm 0.55 | 2.09 \pm 0.77 | 2.10 \pm 0.69 | 2.23 \pm 0.76 |
| UNETR [†] | Cyclic 2.5D (Ours) | 90.36\pm3.59 | 86.55\pm4.31 | 86.58\pm4.22 | 85.40\pm4.51 | 28.79\pm2.58 | 29.60\pm3.68 | 27.52\pm2.43 | 27.39\pm2.72 | 1.47\pm0.56 | 1.96\pm0.72 | 1.96\pm0.64 | 2.07\pm0.70 |
| | 3D | 89.68 \pm 3.74 | 85.80 \pm 4.44 | 85.80 \pm 4.36 | 84.54 \pm 4.70 | 28.25 \pm 2.39 | 28.82 \pm 3.24 | 27.10\pm2.20 | 27.41 \pm 2.46 | 1.51 \pm 0.50 | 2.10 \pm 0.66 | 2.08 \pm 0.59 | 2.21 \pm 0.66 |
| SwimUNETR [†] | 2.5D | 89.68 \pm 3.64 | 85.77 \pm 4.28 | 85.76 \pm 4.19 | 84.58 \pm 4.47 | 28.34\pm2.27 | 29.16 \pm 3.36 | 27.11 \pm 2.02 | 27.57\pm2.42 | 1.44 \pm 0.46 | 2.01\pm0.61 | 2.03\pm0.54 | 2.14\pm0.61 |
| | Cyclic 2.5D (Ours) | 89.93\pm3.27 | 86.03\pm3.92 | 86.07\pm3.89 | 84.84\pm4.18 | 28.34\pm2.51 | 29.32\pm3.65 | 27.13\pm2.29 | 27.57\pm2.63 | 1.44\pm0.52 | 2.04 \pm 0.71 | 2.03 \pm 0.63 | 2.16 \pm 0.70 |
| CycleGAN [†] | 3D | 90.20 \pm 3.68 | 86.42 \pm 4.44 | 86.45 \pm 4.29 | 85.26 \pm 4.64 | 28.28 \pm 2.64 | 29.08 \pm 3.72 | 27.12 \pm 2.38 | 27.46 \pm 2.76 | 1.49 \pm 0.56 | 2.11 \pm 0.83 | 2.08 \pm 0.69 | 2.21 \pm 0.78 |
| | 2.5D | 90.23 \pm 3.55 | 86.42 \pm 4.35 | 86.51 \pm 4.19 | 85.30 \pm 4.53 | 28.60\pm2.58 | 29.47 \pm 3.61 | 27.37 \pm 2.41 | 27.86\pm2.72 | 1.97 \pm 0.73 | 1.98 \pm 0.66 | 2.09 \pm 0.71 | |
| CycleGAN [†] | Cyclic 2.5D (Ours) | 90.29\pm3.40 | 86.57\pm4.11 | 86.69\pm4.01 | 85.36\pm4.38 | 28.52 \pm 2.59 | 29.47\pm3.59 | 27.41\pm2.35 | 27.72 \pm 2.71 | 1.39\pm0.53 | 1.97\pm0.76 | 1.95\pm0.64 | 2.08\pm0.72 |
| | None | 84.69 \pm 4.81 | 79.19 \pm 5.58 | 78.49 \pm 5.40 | 76.94 \pm 5.75 | 26.12 \pm 2.39 | 26.70 \pm 3.16 | 24.75 \pm 2.22 | 25.25 \pm 2.51 | 1.97 \pm 0.66 | 2.76 \pm 0.86 | 2.81 \pm 0.80 | 2.96 \pm 0.89 |
| Pix2Pix [†] | 3D | 85.63 \pm 5.03 | 80.58 \pm 5.67 | 79.84 \pm 5.65 | 78.39 \pm 5.98 | 26.34 \pm 2.38 | 26.87 \pm 3.17 | 24.99 \pm 2.20 | 25.45 \pm 2.55 | 1.94 \pm 0.70 | 2.71 \pm 0.88 | 2.76 \pm 0.83 | 2.92 \pm 0.93 |
| | 2.5D | 87.15 \pm 4.32 | 82.28 \pm 5.01 | 82.16 \pm 4.89 | 80.75 \pm 5.14 | 27.18\pm2.45 | 27.71\pm3.26 | 25.91\pm2.24 | 26.27\pm2.51 | 1.69\pm0.58 | 2.39\pm0.77 | 2.38\pm0.68 | 2.51\pm0.76 |
| CycleGAN [†] | Cyclic 2.5D (Ours) | 87.69\pm3.97 | 82.82\pm4.78 | 82.78\pm4.62 | 81.27\pm4.95 | 27.10 \pm 2.32 | 27.62 \pm 3.21 | 25.90 \pm 2.19 | 26.24 \pm 2.43 | 1.78 \pm 0.56 | 2.46 \pm 0.76 | 2.47 \pm 0.69 | 2.60 \pm 0.74 |
| | None | 82.69 \pm 4.39 | 76.73 \pm 5.05 | 76.35 \pm 4.83 | 74.56 \pm 5.20 | 26.48 \pm 2.01 | 26.56 \pm 2.48 | 25.14 \pm 1.82 | 25.40 \pm 2.06 | 2.05 \pm 0.53 | 2.77 \pm 0.67 | 2.80 \pm 0.63 | 2.93 \pm 0.69 |
| CycleGAN [†] | 3D | 84.10 \pm 4.72 | 78.02 \pm 5.30 | 77.82 \pm 5.11 | 75.90 \pm 5.49 | 26.47 \pm 2.14 | 26.48 \pm 2.62 | 25.12 \pm 1.90 | 25.35 \pm 2.20 | 2.13 \pm 0.71 | 2.84 \pm 0.81 | 2.87 \pm 0.79 | 3.02 \pm 0.86 |
| | 2.5D | 86.66 \pm 4.08 | 81.41 \pm 4.74 | 81.45 \pm 4.54 | 79.72 \pm 4.85 | 27.06 \pm 2.12 | 27.41 \pm 2.90 | 25.74 \pm 1.95 | 26.02 \pm 2.23 | 1.83 \pm 0.61 | 2.52 \pm 0.73 | 2.53 \pm 0.70 | 2.65 \pm 0.76 |
| CycleGAN [†] | Cyclic 2.5D (Ours) | 87.63\pm3.91 | 82.65\pm4.63 | 82.67\pm4.45 | 81.08\pm4.74 | 27.55\pm2.21 | 28.18\pm3.24 | 26.25\pm1.99 | 26.66\pm2.34 | 1.61\pm0.52 | 2.27\pm0.67 | 2.28\pm0.61 | 2.40\pm0.68 |

Table 2: Comprehensive quantitative evaluation of the cyclic 2.5D perceptual loss. The results are presented as mean \pm standard deviation. Models marked with the dagger symbol (\dagger) were trained on datasets preprocessed using by-manufacturer standardization, which standardizes tau PET SUVR values according to manufacturer. In contrast, models without the dagger symbol were trained on datasets preprocessed using min-max normalization. Under min-max normalization, SUVR values are scaled differently depending on the method: PASTA (row 1) (Li et al., 2024) scales SUVR values to the range (0, 1), while ShareGAN (row 2) (Wang et al., 2024) and U-Net (row 3) scale them to the range (-1, 1). Given that the SUVR value ranges differ between PET images preprocessed using by-manufacturer standardization and those preprocessed using min-max normalization, the NMAE is reported instead of the MAE to enable fair comparisons across preprocessing methods. The NMAE is computed by normalizing the MAE with respect to the ground truth PET (y) SUVR values. Note: Overall (3D) refers to the average 3D SSIM, PSNR, or NMAE, while Axial/Coronal/Sagittal corresponds to the average 2D SSIM, PSNR, or NAME calculated for slices 20 to 90 in the axial, coronal, and sagittal planes, respectively.

| Ablation | Preprocessing | | | SSIM(%) \uparrow | PSNR(dB) \uparrow |
|---------------------|---------------|--------------|--------------|----------------------------------|----------------------------------|
| | N3Norm | FSNorm | Skull | | |
| w/o N3Norm & FSNorm | | | \checkmark | 90.28 \pm 3.53 | 28.88\pm2.59 |
| w/o FSNorm | | \checkmark | \checkmark | 90.23 \pm 3.55 | 28.81 \pm 2.49 |
| w/o Skull | \checkmark | \checkmark | | 51.92 \pm 9.69 | 18.35 \pm 1.92 |
| Ours | \checkmark | \checkmark | \checkmark | 90.36\pm3.59 | 28.79 \pm 2.58 |

Table 3: Quantitative comparisons of tau PET synthesis on the test dataset processed using the original and the modified preprocessing pipelines. Image translation was performed using a 3D U-Net model trained with the proposed combined loss function. The results are presented as mean \pm standard deviation. The abbreviations are defined as follows: w/o N3Norm indicates the absence of N3 normalization and FreeSurfer intensity normalization on MRI; w/o FSNorm refers to the absence of FreeSurfer intensity normalization on MRI; and w/o Skull denotes the absence of skull stripping on both MRI and PET data. Note: The SSIM and PSNR values represent evaluations of the entire 3D image volume.

A.3. ROI Analysis Across All Cortical Regions

Figure 1 illustrates the results of an ROI analysis conducted across all cerebral cortex regions, ranked in descending order based on the mean ground truth PET SUVR averaged across the study participants. Notably, the cyclic 2.5D perceptual loss achieves a higher reduction in mean squared error (MSE) in 63 out of the 72 regions when compared to both the 2.5D and 3D perceptual losses. These findings indicate that the cyclic 2.5D perceptual loss exhibits superior performance in modeling Alzheimer’s tau pathology, which primarily affects cortical regions (gray matter), compared to the conventional 2.5D and 3D perceptual approaches.

A.4. Ablation Study on Preprocessing Steps

An ablation study was performed to evaluate the effectiveness of each step in the preprocessing pipeline. Datasets processed with the complete preprocessing pipeline were compared to those processed with certain components removed. In detail, we applied the proposed combined loss function to datasets excluding N3 normalization and initial MRI intensity normalization, initial MRI intensity normalization, and skull stripping. The results are presented in Table 3. Based on our assessment that SSIM is a more suitable metric for evaluating tau PET synthesis, as it reflects perceptual similarity aligned with the human visual system more effectively than PSNR, which calculates pixel-level errors, we selected SSIM as the primary evaluation metric. The dataset processed using the complete pipeline achieved the highest SSIM score, and this fully processed dataset was utilized for model training and evaluation.

References

Çiçek, Ö., Abdulkadir, A., Lienkamp, S.S., Brox, T., Ronneberger, O., 2016. 3d u-net: learning dense volumetric segmentation from sparse annotation, in: Medical Image Computing and Computer-Assisted Intervention–MICCAI 2016: 19th International Conference, Athens, Greece, October 17-21, 2016, Proceedings, Part II 19, Springer. pp. 424–432. doi:10.1007/978-3-319-46723-8_49.

- Li, Y., Yakushev, I., Hedderich, D.M., Wachinger, C., 2024. Pasta: Pathology-aware mri to pet cross-modal translation with diffusion models, in: International Conference on Medical Image Computing and Computer-Assisted Intervention, Springer. pp. 529–540.
- Simonyan, K., Zisserman, A., 2015. Very deep convolutional networks for large-scale image recognition, in: 3rd International Conference on Learning Representations.
- Wang, C., Piao, S., Huang, Z., Gao, Q., Zhang, J., Li, Y., Shan, H., Initiative, A.D.N., et al., 2024. Joint learning framework of cross-modal synthesis and diagnosis for alzheimer’s disease by mining underlying shared modality information. *Medical Image Analysis* 91, 103032.